A model-based dynamic characteristics analysis of a coupled multi-crack rotor system

Libo Xiong · Chunrong Hua · Lumei Lv ·Dawei Dong ·Huajiang Ouyang

Abstract The model-based method plays an essential role in crack detection of rotor systems. To improve the reliability and accuracy of model-based method in rotor crack detection, this paper proposes a coupled multi-crack rotor model by considering the coupling effect between cracks under complex excitations as additional flexibility. The systemic stiffness matrix is derived based on the Timoshenko beam theory and fracture mechanics, in which a detailed description of the coupling mechanism between cracks is presented. The systemic stiffness variation with rotation angles and the effects of crack orientation angles, unbalance orientation angles, and crack depths on dynamic characteristics of the coupled multi-crack rotor are analysed at 1/3 and 1/2 subcritical speeds. The complex nonlinearity induced by the coupling effect between cracks is responsible for the dynamic differences between the coupled and uncoupled models of a multi-crack rotor. The magnitudes of most of 2X and 3X components (X is the rotating frequency of rotor system) of the coupled rotor model are nearly twice as those of the uncoupled model. The prominent super-harmonic components and orbits' morphological features of the coupled multi-crack rotor model are shown to be suitable for early crack detection and crack parameter identification. The theoretical findings of the proposed coupled model show an excellent agreement with the experimental results. This work can give confidence in the applications of the model-based method in health monitoring and multi-crack detection for actual rotors.

Keywords *coupled multi-crack rotor ·coupling effect between cracks · nonlinear stiffness variation ·crack orientation angle ·unbalance orientation angle ·early crack detection*

L. Xiong ·C. Hua (✉) ·L. Lv ·D. Dong
School of Mechanical Engineering, Southwest Jiaotong University, Chengdu, Sichuan 610031, China
e-mail: hcrong@swjtu.cn

H. Ouyang
School of Engineering, University of Liverpool, Liverpool L69 3GH, UK

1 Introduction

Cracks in rotors may cause unexpected catastrophic failure of equipment and expensive maintenance cost. Hence, the timely detection of cracks is of vital significance to maintain healthy and stable operations of rotors. The common crack detection methods can be broadly categorised as the model-based [1], the signal-based [2], and the artificial intelligence-based methods [3]. The model-

based method can conveniently model rotor faults (such as crack, misalignment, eccentricity and rub impact) and realize fault diagnosis by studying the relationship between fault parameters and system dynamics. In addition, the model-based method can also generate dynamic responses in different signal-to-noise ratios, different load conditions and different fault combinations at low cost, which can provide different kinds of data for the signal-based method and the artificial intelligence-based method. Thus, the applications of the model-based method in fault diagnosis and structural health monitoring are still an active research topic in the study of rotating machinery [1, 4].

In the model-based method, cracks are usually modelled as additional equivalent loads [5-7], rotational springs [8-13], and stiffness variation [14-22] in the finite element (FE) model. Considering the crack-induced changes as equivalent loads in a cracked rotor model, Sekhar [5] identified crack depths and locations by minimising the error between measured equivalent forces and the theoretical ones through the modal expansion method and least-square fitting. Pennacchi et al. [6] sought the minimum error of the harmonic component amplitudes in simulated and experimental signals by the least-square identification method to determine crack position and depth. Singh et al. [7] proposed a method to identify crack and bearing parameters of a flexible rotor system through the vibration displacements and active magnetic bearing current signals. Based on the rotational spring model of cracks, the transfer matrix method was applied to the natural frequency analysis of a multi-crack beam [8]. El Arem [9] analysed the nonlinear dynamics, instability and chaotic behavior of a rotating shaft with a switching crack based on the Floquet's theory, Poincaré maps and bifurcation diagrams. A high-precision modal parameter identification method and a wavelet FE model were employed to determine crack parameters [10]. Some investigators [11, 12] used the changes in natural frequencies to detect locations and sizes of multiple cracks in a beam. Lee [13] identified multiple cracks in a beam using the amplitude changes of forced vibration, and obtained crack locations and sizes by the Newton–Raphson iteration method and singular value decomposition method.

Compared with the additional equivalent loads and rotational springs, the approach regarding the crack effects as stiffness variation is widely used in dynamic analysis and crack identification of rotors, which can accurately depict different types of cracks (longitudinal crack, transverse crack, slant crack, open/breathing crack) in system model. AL-Shudeifat [14] conducted research on systemic stability and backward whirl of a rotor with an open crack through the harmonic balance method. The influences of crack depth, shaft slenderness ratio, and rotating speed ratio on system dynamics were revealed based on a cracked Jeffcott rotor model accounting for the

contribution of general transverse forces to the mode I crack [16]. Fu et al. [17] investigated the effects of interval uncertain parameters on the dynamic behaviors of a cracked rotor, and established a surrogate model to quantify the bounds of nonlinear dynamic responses. Xiang et al. [19] analysed the nonlinear crack characteristics of different multi-fault rotors and developed a crack detection method based on orbit characteristics. The squared gains of vibration amplitude were presented to detect cracks and eliminate the influence of adverse disturbances based on auto-correlation and power spectral density functions of rotor vibrations [20]. The natural frequencies for bending vibration in both horizontal and vertical planes were used to detect and locate cracks in non-rotating rotors [21].

As to the model of multi-crack systems, the crack effects are usually treated as the changes in physical properties (stiffness variation, additional equivalent load and rotational spring) of the corresponding cracked element in many literatures. Arem [23] handled the crack influence through the stiffness loss of cracked element and discussed the nonlinear dynamics of a cantilever beam with two cracks under bending moment. Khorrami et al [15] regarded the crack effects as the stiffness variation for a two-crack rotor system, and investigated the effects of crack parameters such as depths, locations and relative angular positions on critical speeds and axis orbit under unbalance and gravitational forces. Sekhar [22] treated cracks by local flexibility changes and estimated the crack depths and locations of a double-crack shaft based on modal expansion approach. Morassi and Rollo [11] used two equivalent massless rotational springs to simulate two cracks in a beam under bending moment. Patil and Maiti [12] modelled cracks by rotational springs and determined the locations and sizes of multiple open cracks in beams under different support conditions. The foregoing researches all neglected the interaction between cracks, reducing the accuracy of cracked rotor system model.

The coupling mechanism between cracks in rotors has still attracted the attentions of some scholars [15]. Darpe et al. [18] considered the interaction of two cracks as the additional flexibility in both lateral directions, and studied the influence of crack orientation angles and unbalance orientation angles on the nonlinear dynamics of a Jeffcott rotor under the gravity and unbalance forces. Li et al. [24] modelled cracks as the contact between two adjacent crack surfaces in the FE mesh model for a cantilever beam with multiple cracks, in which the crack coupling effect was considered as the displacement, strain and stress among cracked element nodes. Zhao et al. [25, 26] used the Green's functions to describe the interaction between cracks, and simulated cracks by rotational and transversal springs for a weaken beam under a harmonic concentrated force.

The above model-based researches have significant efficiency advantages in rotor

dynamic analysis and crack detection. The model-based method demands a reliable system model, which requires accurate modelling of various faults and coupled faults. Rotors in actual harsh environments are often subjected to complex excitations such as bending moments, torques, unbalance and axial impulse forces, increasing the difficulty of system modelling. For this reason, the coupling effect between cracks in rotors under complex excitations has still not been expounded in detail, which greatly limits the application and popularization of the model-based method in fault diagnosis of multi-crack rotors. Aiming at this situation, this paper proposed a coupled multi-crack rotor model by considering the coupling mechanism between cracks under complex excitations as additional flexibility. The stiffness matrix in the equations of motion is derived based on the Timoshenko beam theory and fracture mechanics, containing the additional stiffness variation produced by the multi-crack coupling effect. Then the systemic stiffness variation with rotation angles and the rotor dynamic characteristics with respect to different crack orientation angles, unbalance orientation angles and crack depths are analysed. Finally, a preliminary experimental investigation is conducted to validate the proposed coupled multi-crack rotor model.

2 Coupled multi-crack rotor modelling

The rotor system is composed of a shaft with two transverse breathing cracks (crack-1 and crack-2), two discs and two ball bearings, as shown in Fig. 1(a). Figures 1(b)-(d) depict the coordinate system of two cracks, the load diagram of a cracked shaft element, and the cross section of a crack. In order to maintain the consistency between simulation and experiment, the physical parameters of rotor system selected in this paper are given in Table 1. The Rayleigh damping coefficients a and b are calculated by assuming that the modal damping ratios of the first two modes are 0.005 and 0.01, respectively [27]. And the first critical speed is obtained from the stiffness and mass of an uncracked rotor. In order to accurately describe the variation of crack section with crack breathing, while considering the computational complexity and model accuracy, the crack closure line method [28] is adopted to model the breathing crack in this paper with an assumption that the crack surface is flat and the crack tip is a straight line.

2.1 Equations of motion

The cracked shaft is discretized into 60 Timoshenko beam elements with length of l and radius of R, each element contains two nodes having six degrees of freedom each. A cracked shaft element is shown in Fig. 1(c). The

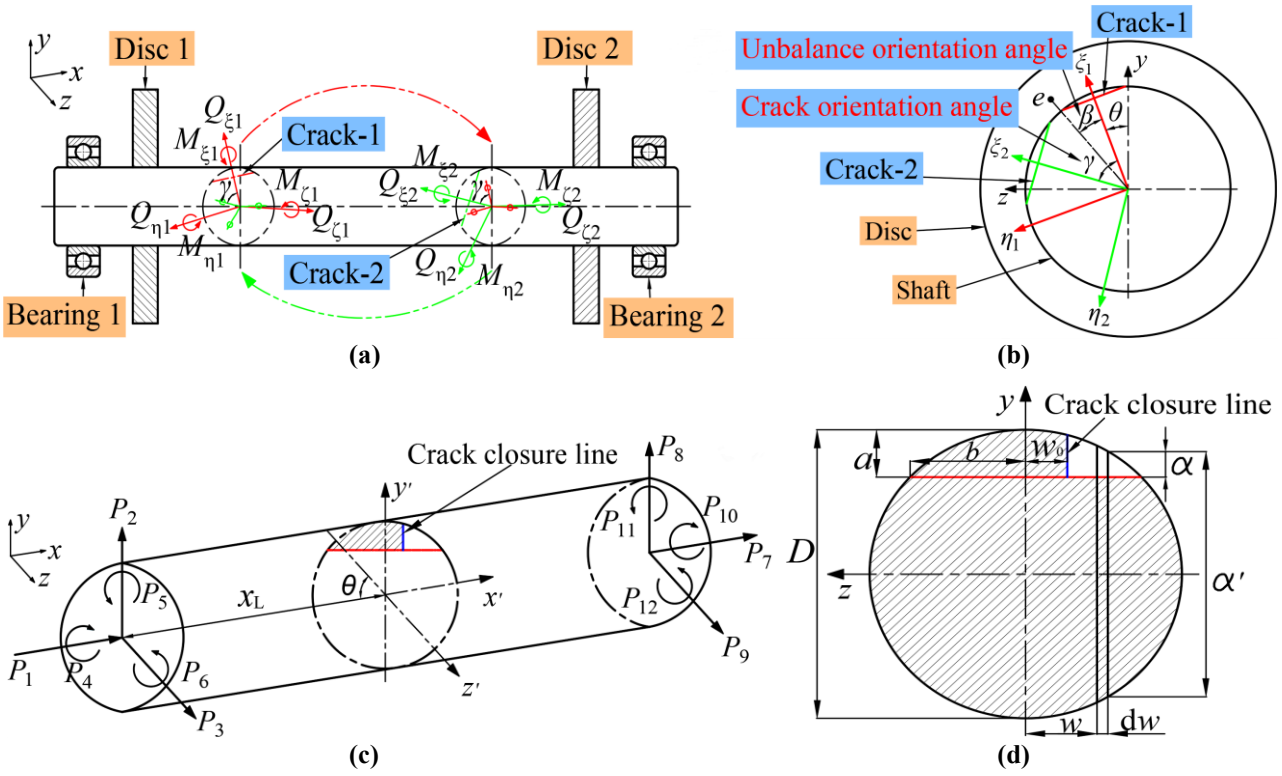

Fig. 1 Model of coupled multi-crack rotor system: **a** system details, **b** coordinate system of two cracks, **c** load diagram of cracked shaft element, **d** cross section of crack

Table 1 Physical parameters of rotor system

Parameter	Value	Parameter	Value
Shaft diameter, D	0.01 m	Polar moment of inertia of disc 1	5.76×10^{-4} kg·m^2
Density of shaft (40Cr)	7.87×10^{3} kg·m^{-3}	Diametrical moment of inertia of disc 1	3.18×10^{-4} kg·m^2
Shaft length	0.6 m	Polar moment of inertia of disc 2	5.84×10^{-4} kg·m^2
Young's modulus, E	2.11×10^{11} N·m^{-2}	Diametrical moment of inertia of disc 2	3.23×10^{-4} kg·m^2
Shear modulus, S_m	8.26×10^{10} N·m^{-2}	Disc eccentricity	2.0×10^{-5} m
Poisson's ratio, v	0.277	Rayleigh damping coefficient, a	0.684
Gravitational acceleration	9.8 m·s^{-2}	Rayleigh damping coefficient, b	2.80×10^{-5}
Mass of disc 1	0.759 kg	First critical speed, Ω_0	3229 rpm
Mass of disc 2	0.770 kg		

two discs are regarded as rigid bodies with three translational and three rotational inertias, added to the mass matrix of the corresponding beam elements. The ball bearings are simplified as springs and dampers to constrain the two lateral degrees of freedom at corresponding nodes. The equations of motion for a coupled multi-crack rotor system in a stationary coordinate system can be expressed as [27]:

$$\mathbf{M}\ddot{\mathbf{q}}+(\mathbf{D}+\Omega\mathbf{D}_g)\dot{\mathbf{q}}+\mathbf{K}\mathbf{q}=\mathbf{F} \tag{1}$$

where $\mathbf{M}$ is the systemic mass matrix, including the shaft mass matrix and the disc mass matrix. $\mathbf{D}=a\mathbf{M}+b\mathbf{K}$ the systemic Rayleigh damping

matrix, Ω the systemic rotational speed, **D**g the systemic gyroscopic matrix, **K** is the systemic stiffness matrix. **F** is the load vector containing the systemic unbalance force, gravity, and external excitations (including bending moments, torques and so on). The systemic displacement vector **q** is denoted as:

$$\mathbf{q} = \left\{ \mathbf{q}_1, \mathbf{q}_2, \cdots, \mathbf{q}_k, \cdots, \mathbf{q}_{Num} \right\}^{\mathrm{T}} \tag{2}$$

where $\mathbf{q}_k = \left\{ u_1, u_2, u_3, u_4, u_5, u_6 \right\}_k^{\mathrm{T}}$ represents the displacement vector of the *k*-th node, *Num* is the number of nodes.

The Newmark method [29] is applied to solve the equations of motion numerically, i.e. computing the variables of $\ddot{\mathbf{q}}$, $\dot{\mathbf{q}}$, **q** in Eq. (1). The specific iterative process is detailed in Ref. [29] with a computational complexity of $O(s)$, where *s* denotes the number of executors in the iterative process. In addition, the Newmark integration constants B_{N} and R_{N} are set as 0.25 and 0.5 to insure the stability and convergence rate of the algorithm. Here, the convergence condition is that the response difference of two adjacent iteration steps (Δt = 0.001 s) is less than the tolerance (1.0×10^{-11}). It should be stated that the stiffness and damping matrices and the excitation terms are constantly updated with crack breathing during the calculation process.

2.2 Stiffness matrix

The two cracks with a crack orientation angle γ (the relative angle between cracks) in Fig. 1(b) are assumed to be sufficiently apart to keep their stress fields independent [18], which implies that the stress field of one crack will not affect that of the other. $\mathbf{F}^{1\,\mathrm{c}}$, $\mathbf{F}^{2\,\mathrm{c}}$ are the load vectors acting on the crack-1 and crack-2 cross-sections in Fig. 1(a), which contain three translational forces and three moments each.

$$\mathbf{F}^{1\,\mathrm{c}} = \left\{ Q_{\zeta 1}, Q_{\xi 1}, Q_{\eta 1}, M_{\zeta 1}, M_{\xi 1}, M_{\eta 1} \right\}^{\mathrm{T}} \tag{3}$$

$$\mathbf{F}^{2\,\mathrm{c}} = \left\{ Q_{\zeta 2}, Q_{\xi 2}, Q_{\eta 2}, M_{\zeta 2}, M_{\xi 2}, M_{\eta 2} \right\}^{\mathrm{T}} \tag{4}$$

From the equilibrium of the forces in the elements containing crack-1 and crack-2 and the coordinate system of two cracks in Fig. 1(b), $\mathbf{F}^{2\,\mathrm{c}}$ can be expressed by $\mathbf{F}^{1\,\mathrm{c}}$ [18]:

$$\mathbf{F}^{2\,\mathrm{c}} = \mathbf{T}^{\mathrm{cp}} \mathbf{F}^{1\,\mathrm{c}} \tag{5}$$

where $\mathbf{T}^{\mathrm{cp}}$ is named as the coupling matrix between $\mathbf{F}^{1\,\mathrm{c}}$ and $\mathbf{F}^{2\,\mathrm{c}}$.

$$\mathbf{T}^{\mathrm{cp}} = \begin{bmatrix} 1 & 0 & 0 & 0 & 0 & 0 \\ 0 & \cos\gamma & \sin\gamma & 0 & 0 & 0 \\ 0 & -\sin\gamma & \cos\gamma & 0 & 0 & 0 \\ 0 & 0 & 0 & 1 & 0 & 0 \\ 0 & 0 & 0 & 0 & \cos\gamma & \sin\gamma \\ 0 & 0 & 0 & 0 & -\sin\gamma & \cos\gamma \end{bmatrix} \tag{6}$$

Considering the interaction of the two cracks (the coupling effect between cracks), the additional displacement vector $\mathbf{q}^{2\sim 1\,\mathrm{c}}$ due to crack-1 at crack-2 is written as [18]:

$$\mathbf{q}^{2\sim 1\,\mathrm{c}} = \mathbf{T}^{\mathrm{cp}} \mathbf{q}^{1\,\mathrm{c}} \tag{7}$$

where $\mathbf{q}^{1\,\mathrm{c}}$ is the additional displacement vector resulted from crack-1 at crack-1:

$$\mathbf{q}^{1\,\mathrm{c}} = \left\{ u_1^{1\,\mathrm{c}}, u_2^{1\,\mathrm{c}}, u_3^{1\,\mathrm{c}}, u_4^{1\,\mathrm{c}}, u_5^{1\,\mathrm{c}}, u_6^{1\,\mathrm{c}} \right\}^{\mathrm{T}} \tag{8}$$

So the total displacement vector at crack-2 is written as:

$$\hat{\mathbf{q}}^{2} = \mathbf{q}^{2\,0} + \mathbf{q}^{2\,\mathrm{c}} + \mathbf{q}^{2\sim1\,\mathrm{c}} \tag{9}$$

where $\mathbf{q}^{2\,0}$ is the displacement vector of the uncracked element and $\mathbf{q}^{2\,\mathrm{c}}$ is the additional displacement vector at crack-2, expressed as follows:

$$\mathbf{q}^{2\,0} = \left\{u_1^{2\,0}, u_2^{2\,0}, u_3^{2\,0}, u_4^{2\,0}, u_5^{2\,0}, u_6^{2\,0}\right\}^{\mathrm{T}} \tag{10}$$

$$\mathbf{q}^{2\,\mathrm{c}} = \left\{u_1^{2\,\mathrm{c}}, u_2^{2\,\mathrm{c}}, u_3^{2\,\mathrm{c}}, u_4^{2\,\mathrm{c}}, u_5^{2\,\mathrm{c}}, u_6^{2\,\mathrm{c}}\right\}^{\mathrm{T}} \tag{11}$$

Considering the axial forces, bending moments and torques, and shear forces in the element containing crack-2, the total displacement at crack-2 in the *i*-th direction can be obtained from Castigliano's theorem, expressed as:

$$\begin{aligned} u_i^2 &= \frac{\partial U^2}{\partial P_i^{2\,\mathrm{c}}} = \frac{\partial}{\partial P_i^{2\,\mathrm{c}}}(U^{2\,0} + U^{2\,\mathrm{c}} + U^{2\sim1\,\mathrm{c}}) \\ &= u_i^{2\,0} + u_i^{2\,\mathrm{c}} + u_i^{2\sim1\,\mathrm{c}} \end{aligned} \tag{12}$$

where $u_i^{2\,0}$ the displacement of the uncracked element, $u_i^{2\,\mathrm{c}}$ the additional displacement at crack-2, $u_i^{2\sim1\,\mathrm{c}}$ the additional displacement due to crack-1 at crack-2, $P_i^{2\,\mathrm{c}}$ the load at the crack-2 cross-section along the *i*-th coordinate; *i* = 1-6. U^2 is the total strain energy at crack-2, $U^{2\,0}$ the strain energy of the uncracked shaft element, $U^{2\,\mathrm{c}}$ the additional strain energy resulted from crack-2 at crack-2, $U^{2\sim1\,\mathrm{c}}$ the additional strain energy due to crack-1 at crack-2; in which the detailed expressions of $U^{2\,0}$ and $U^{2\,\mathrm{c}}$ can be found in Ref. [28].

According to the fracture mechanics concepts, the additional strain energy of crack-2 considering the coupling effect between the two cracks can be expressed as

$$U^{2\sim1\,\mathrm{c}} = \int_{A^{2\,\mathrm{c}}} J_{2\sim1}(A^{\mathrm{c}})\,\mathrm{d}A^{\mathrm{c}} \tag{13}$$

where A^{c} is the area of crack region, $A^{2\,\mathrm{c}}$ the area of crack region at crack-2. $J_{2\sim1}(A^{\mathrm{c}})$ is the homologous strain energy density function, denoted as

$$\begin{aligned} J_{2\sim1}(A^{\mathrm{c}}) = \frac{1}{E'}\Bigg[&\Big(\sum_{i=1}^{6} K_i^{\mathrm{I}}\Big)^2 + \Big(\sum_{i=1}^{6} K_i^{\mathrm{II}}\Big)^2 \\ &+ m_s\Big(\sum_{i=1}^{6} K_i^{\mathrm{III}}\Big)^2 \Bigg]_{2\sim1} \end{aligned} \tag{14}$$

where $E' = E/(1-\nu)$ and $m_s = 1+\nu$, ν is the Poisson ratio. K_i^{I}, K_i^{II} and K_i^{III} are the relevant stress intensity factors along the crack edge of crack-2, corresponding to the opening, sliding and tearing modes of crack displacement (detailed in Ref. [28]). These stress intensity factors only depend on stresses acting on the crack edge of crack-2, and the magnitudes of which will not be affected by the stresses at crack-1 for the independence of the stress fields at the two cracks.

Next, the flexibility coefficient g_{ij}^2 at crack-2 is derived as:

$$\begin{aligned} g_{ij}^2 &= \frac{\partial u_i^2}{\partial P_j^{2\,\mathrm{c}}} = \frac{\partial}{\partial P_j^{2\,\mathrm{c}}}(u_i^{2\,0} + u_i^{2\,\mathrm{c}} + u_i^{2\sim1\,\mathrm{c}}) \\ &= g_{ij}^{2\,0} + g_{ij}^{2\,\mathrm{c}} + g_{ij}^{2\sim1\,\mathrm{c}} \end{aligned} \tag{15}$$

where $P_j^{2\,\mathrm{c}}$ is the load at the crack-2 cross-section along the *j*-th coordinate. $g_{ij}^{2\,0}$, $g_{ij}^{2\,\mathrm{c}}$, $g_{ij}^{2\sim1\,\mathrm{c}}$ are the flexibility coefficients of the uncracked element, the additional flexibility coefficient at crack-2, and the additional

flexibility coefficient due to crack-1 at crack-2; j = 1-6.

The flexibility coefficients $g_{ij}^{2\,0}$ and $g_{ij}^{2\,c}$ can be found in detail from [28] based on strain energy release rate theory [30]. Consequently, the flexibility matrix $\mathbf{G}^{2\,0}$ of the uncracked element and the additional flexibility matrix $\mathbf{G}^{2\,c}$ at crack-2 are written as follows:

$$\mathbf{G}^{2\,0}=\begin{bmatrix} \frac{l}{EA} & 0 & 0 & 0 & 0 & 0 \\ 0 & \frac{\alpha_s l}{S_m A}+\frac{l^3}{3EI} & 0 & 0 & 0 & -\frac{l^2}{4EI} \\ 0 & 0 & \frac{\alpha_s l}{S_m A}+\frac{l^3}{3EI} & 0 & \frac{l^2}{4EI} & 0 \\ 0 & 0 & 0 & \frac{l}{EI_0} & 0 & 0 \\ 0 & 0 & \frac{l^2}{4EI} & 0 & \frac{l}{EI} & 0 \\ 0 & -\frac{l^2}{4EI} & 0 & 0 & 0 & \frac{l}{EI} \end{bmatrix} \tag{16}$$

$$\mathbf{G}^{2\,c}=\begin{bmatrix} g_{11}^{2\,c} & g_{12}^{2\,c} & g_{13}^{2\,c} & g_{14}^{2\,c} & g_{15}^{2\,c} & g_{16}^{2\,c} \\ g_{21}^{2\,c} & g_{22}^{2\,c} & g_{23}^{2\,c} & g_{24}^{2\,c} & g_{25}^{2\,c} & g_{26}^{2\,c} \\ g_{31}^{2\,c} & g_{32}^{2\,c} & g_{33}^{2\,c} & g_{34}^{2\,c} & g_{35}^{2\,c} & g_{36}^{2\,c} \\ g_{41}^{2\,c} & g_{42}^{2\,c} & g_{43}^{2\,c} & g_{44}^{2\,c} & g_{45}^{2\,c} & g_{46}^{2\,c} \\ g_{51}^{2\,c} & g_{52}^{2\,c} & g_{53}^{2\,c} & g_{54}^{2\,c} & g_{55}^{2\,c} & g_{56}^{2\,c} \\ g_{61}^{2\,c} & g_{62}^{2\,c} & g_{63}^{2\,c} & g_{64}^{2\,c} & g_{65}^{2\,c} & g_{66}^{2\,c} \end{bmatrix} \tag{17}$$

where l the length of per shaft element, A the area of the shaft cross-section, α_s the shear coefficient, S_m the shear modulus, E Young's modulus, I the area moment of inertia of cross-section, I_0 the polar moment of inertia of cross-section.

The additional flexibility coefficients due to the coupling effect between the two cracks are calculated as per Eq. (15):

$$g_{ij}^{2\sim 1\,c}=\frac{\partial u_i^{2\sim 1\,c}}{\partial P_j^{2\,c}} \tag{18}$$

Here, based upon Eq. (7), $u_i^{2\sim 1\,c}$ satisfy

$$\left\{u_{1-6}^{2\sim 1\,c}\right\}^{\mathrm{T}}=\mathbf{T}^{\mathrm{cp}}\left\{u_{1-6}^{1\,c}\right\}^{\mathrm{T}} \tag{19}$$

where $u_i^{1\,c}$ are the additional displacements at crack-1, expressed as:

$$
\begin{aligned}
u_1^{1\,\mathrm{c}} &= \frac{2}{E'\pi R^4}\iint_{A^{1\,\mathrm{c}}}(\sin^4\theta F_1^2 + m_s\sin^2\theta\cos^2\theta F_{\mathrm{III}}^2)\alpha\mathrm{d}A^{\mathrm{c}}\bullet P_1^{1\,\mathrm{c}} \\
&+ \frac{1}{E'\pi R^6}\iint_{A^{1\,\mathrm{c}}}(4x_s h\sin^4\theta F_1F_2 + 4m_s x_s h\sin^2\theta\cos^2\theta F_{\mathrm{III}}^2)\alpha\mathrm{d}A^{\mathrm{c}}\bullet P_2^{1\,\mathrm{c}} \\
&+ \frac{1}{E'\pi R^6}\iint_{A^{1\,\mathrm{c}}}\begin{pmatrix}2kR^2\sin 2\theta\sin^2\theta F_1^2 + 2kR^2\sin\theta\cos\theta\cos 2\theta F_{\mathrm{III}}^2\\ +8x_s w\sin^5\theta F_1^2 + 8x_s m_s w\sin^3\theta\cos^2\theta F_{\mathrm{III}}^2\end{pmatrix}\alpha\mathrm{d}A^{\mathrm{c}}\bullet P_3^{1\,\mathrm{c}} \\
&+ \frac{1}{E'\pi R^6}\iint_{A^{1\,\mathrm{c}}}(2h\sin 2\theta\sin^2\theta F_1F_2 + 2m_s h\sin\theta\cos\theta\cos 2\theta F_{\mathrm{III}}^2)\alpha\mathrm{d}A^{\mathrm{c}}\bullet P_4^{1\,\mathrm{c}} \\
&+ \frac{2}{E'\pi R^6}\iint_{A^{1\,\mathrm{c}}}(8w\sin^5\theta F_1^2 + 8m_s w\cos^2\theta\sin^3\theta F_{\mathrm{III}}^2)\alpha\mathrm{d}A^{\mathrm{c}}\bullet P_5^{1\,\mathrm{c}} \\
&+ \frac{-1}{E'\pi R^6}\iint_{A^{1\,\mathrm{c}}}(4h\sin^4\theta F_1F_2 + 4m_s h\sin^2\theta\cos^2\theta F_{\mathrm{III}}^2)\alpha\mathrm{d}A^{\mathrm{c}}\bullet P_6^{1\,\mathrm{c}}
\end{aligned}
\tag{20}
$$

$$
\begin{aligned}
u_2^{1\,\mathrm{c}} &= \frac{2}{E'\pi R^8}\iint_{A^{1\,\mathrm{c}}}(4x_s^2h^2\sin^4\theta F_2^2 + 4m_s x_s^2h^2\sin^2\theta\cos^2\theta F_{\mathrm{III}}^2 + k^2R^4\sin^2\theta F_{\mathrm{II}}^2)\alpha\mathrm{d}A^{\mathrm{c}}\bullet P_2^{1\,\mathrm{c}} \\
&+ \frac{1}{E'\pi R^8}\iint_{A^{1\,\mathrm{c}}}\begin{pmatrix}4x_s khR^2\sin 2\theta\sin^2\theta F_2^2 + 4x_s m_s khR^2\sin\theta\cos\theta\cos 2\theta F_{\mathrm{III}}^2\\ +16hwx_s^2\sin^5\theta F_1F_2 + 16m_s hwx_s^2\sin^3\theta\cos^2\theta F_{\mathrm{III}}^2\end{pmatrix}\alpha\mathrm{d}A^{\mathrm{c}}\bullet P_3^{1\,\mathrm{c}} \\
&+ \frac{1}{E'\pi R^8}\iint_{A^{1\,\mathrm{c}}}\begin{pmatrix}4x_s h^2\sin 2\theta\sin^2\theta F_2^2 + 4x_s m_s h^2\sin\theta\cos\theta\cos 2\theta F_{\mathrm{III}}^2\\ +4kwR^2\sin^3\theta F_{\mathrm{II}}^2\end{pmatrix}\alpha\mathrm{d}A^{\mathrm{c}}\bullet P_4^{1\,\mathrm{c}} \\
&+ \frac{1}{E'\pi R^8}\iint_{A^{1\,\mathrm{c}}}(16x_s hw\sin^5\theta F_1F_2 + 16x_s m_s hw\cos^2\theta\sin^3\theta F_{\mathrm{III}}^2)\alpha\mathrm{d}A^{\mathrm{c}}\bullet P_5^{1\,\mathrm{c}} \\
&+ \frac{-2}{E'\pi R^8}\iint_{A^{1\,\mathrm{c}}}(4x_s h^2\sin^4\theta F_2^2 + 4x_s m_s h^2\sin^2\theta\cos^2\theta F_{\mathrm{III}}^2)\alpha\mathrm{d}A^{\mathrm{c}}\bullet P_6^{1\,\mathrm{c}}
\end{aligned}
\tag{21}
$$

$$
\begin{aligned}
u_3^{1\,\mathrm{c}} &= \frac{2}{E'\pi R^8}\iint_{A^{1\,\mathrm{c}}}\begin{pmatrix}k^2R^4\sin^2\theta F_1^2 + m_s k^2R^4\cos^2 2\theta F_{\mathrm{III}}^2 + 16x_s^2w^2\sin^6\theta F_1^2\\ +16m_s x_s^2w^2\cos^2\theta\sin^4\theta F_{\mathrm{III}}^2 + 8kx_s wR^2\sin 2\theta\sin^3\theta F_1^2\\ +8kx_s wR^2\cos\theta\cos 2\theta\sin^2\theta F_{\mathrm{III}}^2\end{pmatrix}\alpha\mathrm{d}A^{\mathrm{c}}\bullet P_3^{1\,\mathrm{c}} \\
&+ \frac{1}{E'\pi R^8}\iint_{A^{1\,\mathrm{c}}}\begin{pmatrix}8x_s hw\sin 2\theta\sin^2\theta F_1F_2 + 8x_s m_s hw\cos\theta\cos 2\theta\sin^2\theta F_{\mathrm{III}}^2\\ +2khR^2\sin^2 2\theta F_1F_2 + 2m_s khR^2\cos^2 2\theta F_{\mathrm{III}}^2\end{pmatrix}\alpha\mathrm{d}A^{\mathrm{c}}\bullet P_4^{1\,\mathrm{c}} \\
&+ \frac{1}{E'\pi R^8}\iint_{A^{1\,\mathrm{c}}}\begin{pmatrix}8kwR^2\sin 2\theta\sin^3\theta F_1^2 + 8m_s kwR^2\cos\theta\cos 2\theta\sin^2\theta F_{\mathrm{III}}^2\\ +32x_s w^2\sin^6\theta F_1^2 + 32x_s m_s w^2\cos^2\theta\sin^4\theta F_{\mathrm{III}}^2\end{pmatrix}\alpha\mathrm{d}A^{\mathrm{c}}\bullet P_5^{1\,\mathrm{c}} \\
&+ \frac{-1}{E'\pi R^8}\iint_{A^{1\,\mathrm{c}}}\begin{pmatrix}4khR^2\sin 2\theta\sin^2\theta F_1F_2 + 4m_s khR^2\sin\theta\cos\theta\cos 2\theta F_{\mathrm{III}}^2\\ +16x_s hw\sin^5\theta F_1F_2 + 16x_s m_s hw\sin^3\theta\cos^2\theta F_{\mathrm{III}}^2\end{pmatrix}\alpha\mathrm{d}A^{\mathrm{c}}\bullet P_6^{1\,\mathrm{c}}
\end{aligned}
\tag{22}
$$

$$u_4^{1\,c}=\frac{2}{E'\pi R^8}\iint_{A^{1\,c}}(h^2\sin^2 2\theta F_2^2+m_s h^2\cos^2 2\theta F_{\mathrm{III}}^2+4w^2\sin^4\theta F_{\mathrm{II}}^2)\alpha\,\mathrm{d}A^{c}\bullet P_4^{1\,c}$$
$$+\frac{1}{E'\pi R^8}\iint_{A^{1\,c}}(8hw\sin 2\theta\sin^3\theta F_1F_2+8m_s hw\cos\theta\cos 2\theta\sin^2\theta F_{\mathrm{III}}^2)\alpha\,\mathrm{d}A^{c}\bullet P_5^{1\,c} \tag{23}$$
$$+\frac{-1}{E'\pi R^8}\iint_{A^{1\,c}}(4h^2\sin 2\theta\sin^2\theta F_2^2+4m_s h^2\sin\theta\cos\theta\cos 2\theta F_{\mathrm{III}}^2)\alpha\,\mathrm{d}A^{c}\bullet P_6^{1\,c}$$

$$u_5^{1\,c}=\frac{2}{E'\pi R^8}\iint_{A^{1\,c}}(16w^2\sin^6\theta F_1^2+16m_s w^2\cos^2\theta\sin^4\theta F_{\mathrm{III}}^2)\alpha\,\mathrm{d}A^{c}\bullet P_5^{1\,c}$$
$$+\frac{-1}{E'\pi R^8}\iint_{A^{1\,c}}(16hw\sin^5\theta F_1F_2+16m_s hw\cos^2\theta\sin^3\theta F_{\mathrm{III}}^2)\alpha\,\mathrm{d}A^{c}\bullet P_6^{1\,c} \tag{24}$$

$$u_6^{1\,c}=\frac{2}{E'\pi R^8}\iint_{A^{1\,c}}(4h^2\sin^4\theta F_2^2+4m_s h^2\sin^2\theta\cos^2\theta F_{\mathrm{III}}^2)\alpha\,\mathrm{d}A^{c}\bullet P_6^{1\,c} \tag{25}$$

where $k=6(1+\nu)/(7+6\nu)$ is the shaft cross-sectional shape coefficient, R the shaft radius (equals $D/2$), θ the torsional angle of a crack relative to the shaft axis, $A^{1\,c}$ the area of crack region at crack-1, $P_j^{1\,c}$ the load at the crack-1 cross-section along the j-th coordinate. α is the crack depth at any distance w from the center along the crack edge. α' is the total height of the strip with width dw, shown in Fig. 1(d). Here $x_s=(x_{\mathrm{L}}+w\cos\theta)$, $h=2\sqrt{R^2-w^2\sin^2\theta}$, and F_1, F_2, F_{II}, F_{III} are denoted as [28]:

$$F_1(\alpha/h)=\sqrt{\frac{2h}{\pi\alpha}\tan(\frac{\pi\alpha}{2h})}\,\frac{0.752+2.02(\alpha/h)+0.37\left[1-\sin(\pi\alpha/2h)\right]^3}{\cos(\pi\alpha/2h)} \tag{26}$$

$$F_2(\alpha/h)=\sqrt{\frac{2h}{\pi\alpha}\tan(\frac{\pi\alpha}{2h})}\,\frac{0.923+0.199\left[1-\sin(\pi\alpha/2h)\right]^4}{\cos(\pi\alpha/2h)} \tag{27}$$

$$F_{\mathrm{II}}(\alpha/h)=\frac{1.122-0.561(\alpha/h)+0.085(\alpha/h)^2+0.18(\alpha/h)^3}{\sqrt{1-(\alpha/h)}} \tag{28}$$

$$F_{\mathrm{III}}(\alpha/h)=\sqrt{\frac{2h}{\pi\alpha}\tan(\frac{\pi\alpha}{2h})} \tag{29}$$

From Eq. (5), $P_j^{2\,c}$ can be expressed by $P_j^{1\,c}$

$$\left\{P_{1-6}^{2\,c}\right\}^{\mathrm{T}}=\mathbf{T}^{\mathrm{cp}}\left\{P_{1-6}^{1\,c}\right\}^{\mathrm{T}} \tag{30}$$

Substituting Eq. (30) into Eqs. (20)-(25), $u_i^{1\,c}$ can be described by $P_j^{2\,c}$, shown in Appendix A.

Consequently, the flexibility coefficients $g_{ij}^{2\sim 1\,c}$ in Eq. (18) can be derived, given in Appendix B. And the flexibility matrix $\mathbf{G}^{2\sim 1\,c}$ is denoted as

$$\mathbf{G}^{2\sim 1\,c}=\begin{bmatrix} g_{11}^{2\sim 1\,c} & g_{12}^{2\sim 1\,c} & g_{13}^{2\sim 1\,c} & g_{14}^{2\sim 1\,c} & g_{15}^{2\sim 1\,c} & g_{16}^{2\sim 1\,c} \\ g_{21}^{2\sim 1\,c} & g_{22}^{2\sim 1\,c} & g_{23}^{2\sim 1\,c} & g_{24}^{2\sim 1\,c} & g_{25}^{2\sim 1\,c} & g_{26}^{2\sim 1\,c} \\ g_{31}^{2\sim 1\,c} & g_{32}^{2\sim 1\,c} & g_{33}^{2\sim 1\,c} & g_{34}^{2\sim 1\,c} & g_{35}^{2\sim 1\,c} & g_{36}^{2\sim 1\,c} \\ g_{41}^{2\sim 1\,c} & g_{42}^{2\sim 1\,c} & g_{43}^{2\sim 1\,c} & g_{44}^{2\sim 1\,c} & g_{45}^{2\sim 1\,c} & g_{46}^{2\sim 1\,c} \\ g_{51}^{2\sim 1\,c} & g_{52}^{2\sim 1\,c} & g_{53}^{2\sim 1\,c} & g_{54}^{2\sim 1\,c} & g_{55}^{2\sim 1\,c} & g_{56}^{2\sim 1\,c} \\ g_{61}^{2\sim 1\,c} & g_{62}^{2\sim 1\,c} & g_{63}^{2\sim 1\,c} & g_{64}^{2\sim 1\,c} & g_{65}^{2\sim 1\,c} & g_{66}^{2\sim 1\,c} \end{bmatrix} \tag{31}$$

The total flexibility matrix of the element containing crack-2 is calculated

$$\mathbf{G}_{\mathrm{ce}}^{2}=\mathbf{G}^{2\,0}+\mathbf{G}^{2\,c}+\mathbf{G}^{2\sim 1\,c} \tag{32}$$

Thus, the stiffness matrix of the element containing crack-2 can be described by the total flexibility matrix:

$$\mathbf{K}_{\mathrm{ce}}^{2}=\mathbf{T}\,(\mathbf{G}_{\mathrm{ce}}^{2})^{-1}\mathbf{T}^{\mathrm{T}} \tag{33}$$

where the transformation matrix $\mathbf{T}$ is given by Ref. [28]

$$\mathbf{T}^{\mathrm{T}}=\begin{bmatrix} 1 & 0 & 0 & 0 & 0 & 0 & -1 & 0 & 0 & 0 & 0 & 0 \\ 0 & 1 & 0 & 0 & 0 & 0 & 0 & -1 & 0 & 0 & 0 & l \\ 0 & 0 & 1 & 0 & 0 & 0 & 0 & 0 & -1 & 0 & -l & 0 \\ 0 & 0 & 0 & 1 & 0 & 0 & 0 & 0 & 0 & -1 & 0 & 0 \\ 0 & 0 & 0 & 0 & 1 & 0 & 0 & 0 & 0 & 0 & -1 & 0 \\ 0 & 0 & 0 & 0 & 0 & 1 & 0 & 0 & 0 & 0 & 0 & -1 \end{bmatrix} \tag{34}$$

It is necessary to note that the crack orientation angle γ is negative in calculating the stiffness matrix $\mathbf{K}_{\mathrm{ce}}^{1}$ of the element containing crack-1 (γ is negative in clockwise and positive in counter-clockwise directions).

Generally, for a multi-crack rotor system (the number of cracks is over 1), the stiffness matrix of any p-th crack element can be given

$$\mathbf{K}_{\mathrm{ce}}^{p}=\mathbf{T}\,(\mathbf{G}_{\mathrm{ce}}^{p})^{-1}\mathbf{T}^{\mathrm{T}} \tag{35}$$

And the flexibility matrix of the p-th crack element $\mathbf{G}_{\mathrm{ce}}^{p}$ is derived as

$$\mathbf{G}_{\mathrm{ce}}^{p}=\mathbf{G}^{p\,0}+\mathbf{G}^{p\,c}+\sum_{q=1,q\neq p}^{n}\mathbf{G}^{p\sim q\,c} \tag{36}$$

where q denotes the q-th crack element, n is the number of cracks (p, $q \le n$). $\mathbf{G}^{p\,0}$ is the flexibility matrix of the uncracked element, $\mathbf{G}^{p\,c}$ is the additional flexibility matrix at crack-p, and $\mathbf{G}^{p\sim q\,c}$ is the additional flexibility matrix due to crack-q at crack-p.

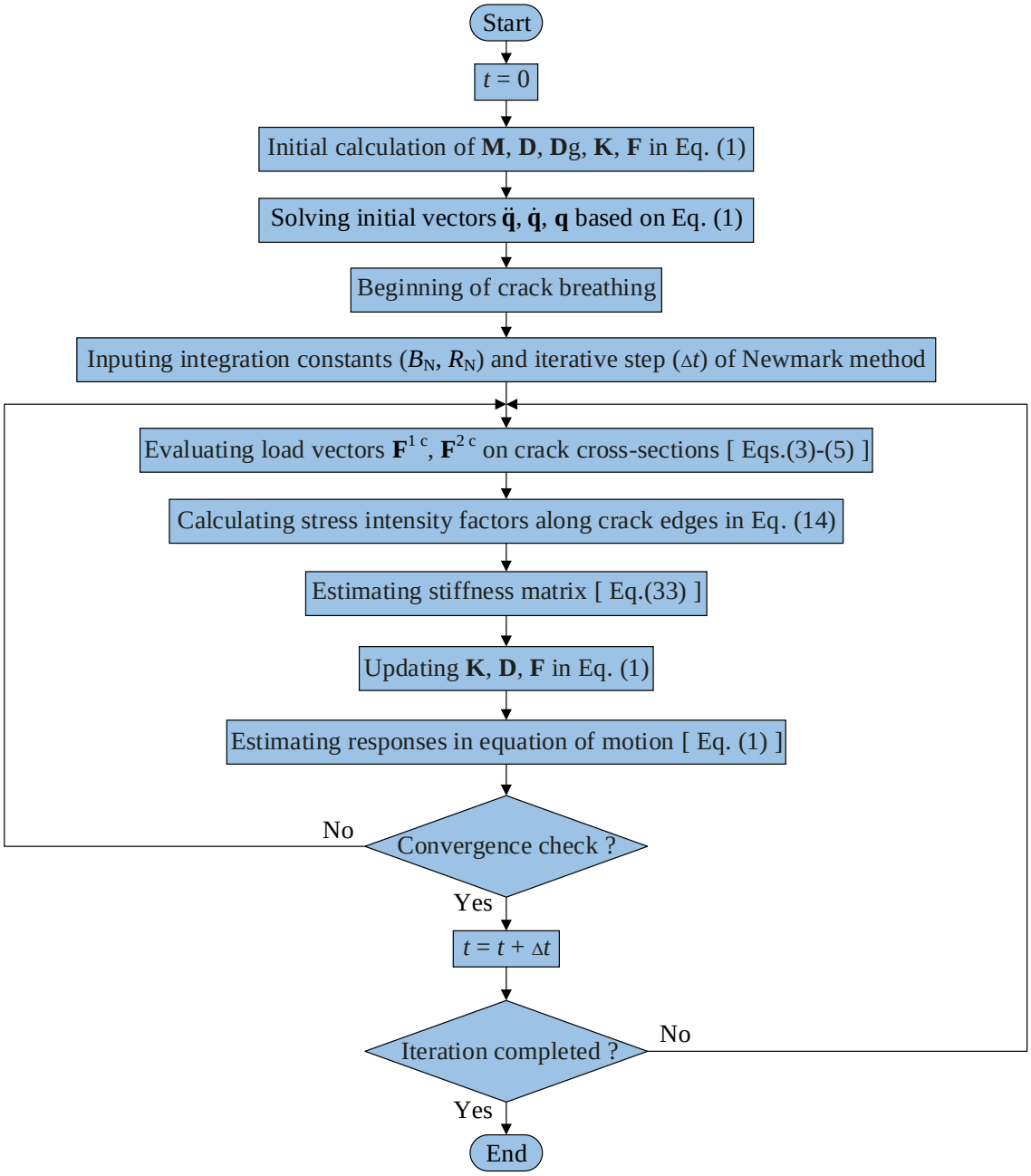

Fig. 2 Flowchart of Newmark method for solving system dynamic responses

The flowchart of the Newmark method for solving the dynamic responses of the coupled multi-crack rotor is shown in Fig. 2. When t = 0 (Initially, the cracks are assumed to close completely), the initial mass matrix **M**, Rayleigh damping matrix **D**, gyroscopic matrix **D**g, stiffness matrix **K** and load vector **F** are calculated from an uncracked rotor. The initial responses $\ddot{\mathbf{q}}$, $\dot{\mathbf{q}}$, **q** also correspond to that of the uncracked rotor. Then the cracks begin to breathe, meanwhile the Newmark method is used to evaluate and update the values of **K**, **D** and **F** in the equation of motion. Based on the above updated **K**, **D** and **F**, the system responses in

each iteration step are calculated until the iteration is completed. Noting that the displacement response $\mathbf{q}$ at crack-2 obtained from Eq. (1) is equal to the total displacement vector $\hat{\mathbf{q}}^2$ in Eq. (9), where the displacement components $\mathbf{q}^{20}$, $\mathbf{q}^{2c}$ and $\mathbf{q}^{2\sim1c}$ are not computed separately, and the same is true for crack-1.

The loads on crack cross-sections and the stiffness of cracked elements will change with crack breathing. When forces at the cross-section of crack-1 begin to change, the corresponding coupling forces acting on the cross-section of crack-2 also change to achieve the force equilibrium of rotor systems, described in Eq. (5). This interaction between the two cracks will increase the displacement and flexibility of the cracked element, found in Eqs. (7) and (18). Therefore, the additional flexibility matrix $\mathbf{G}^{2c}$ due to the crack-2 [15, 27] and the additional flexibility matrix $\mathbf{G}^{2\sim1c}$ (Eq. (31)) caused by the coupling effect between cracks are both considered into the proposed coupled multi-crack rotor model.

Compared with the uncoupled multi-crack rotor model ignoring the interaction between cracks (i.e. $\mathbf{G}^{2\sim1c} = 0$) [15, 27], it can be seen from Eqs. (32)-(33) that the coupling effect between cracks in the coupled multi-crack rotor model under complex excitations further increases the systemic flexibility and alters the systemic time-varying stiffness and Rayleigh damping in Eq. (1). The variation of these physical properties of cracked rotor system will further change the systemic eigenmodes and eigenfrequencies, and aggravate the complexity of nonlinear vibration responses of cracked rotors.

3 Dynamics analysis

The simulated vibration responses of a coupled multi-crack rotor model with different crack orientation angles, unbalance orientation angles (i.e. the relative angle between the eccentricity of discs and the crack-1 direction ξ_1), and crack depths are determined under torsional and unbalance excitations. The stiffness variation, vertical responses and orbits at the 21st node (at disc 1) are analysed and compared with the results of the uncoupled multi-crack rotor model in Refs. [15, 27]. In order to obtain obvious crack fault characteristics, the systemic rotating speeds are $1/3\Omega_0$ and $1/2\Omega_0$ [31, 32] (Ω_0 is the first critical speed of an uncracked rotor model). The two transverse breathing cracks (crack-1 and crack-2) are located in the 26th and 36th elements with a same depth of $0.2D$ (D is the shaft diameter). In the following text, the coupled multi-crack rotor model is referred to as the coupled rotor, and the uncoupled multi-crack rotor model is named the uncoupled rotor. Noting that only the 1X component exists in the frequency spectrum of an uncracked rotor model on account of the systemic stiffness remains unchanged during rotation [28].

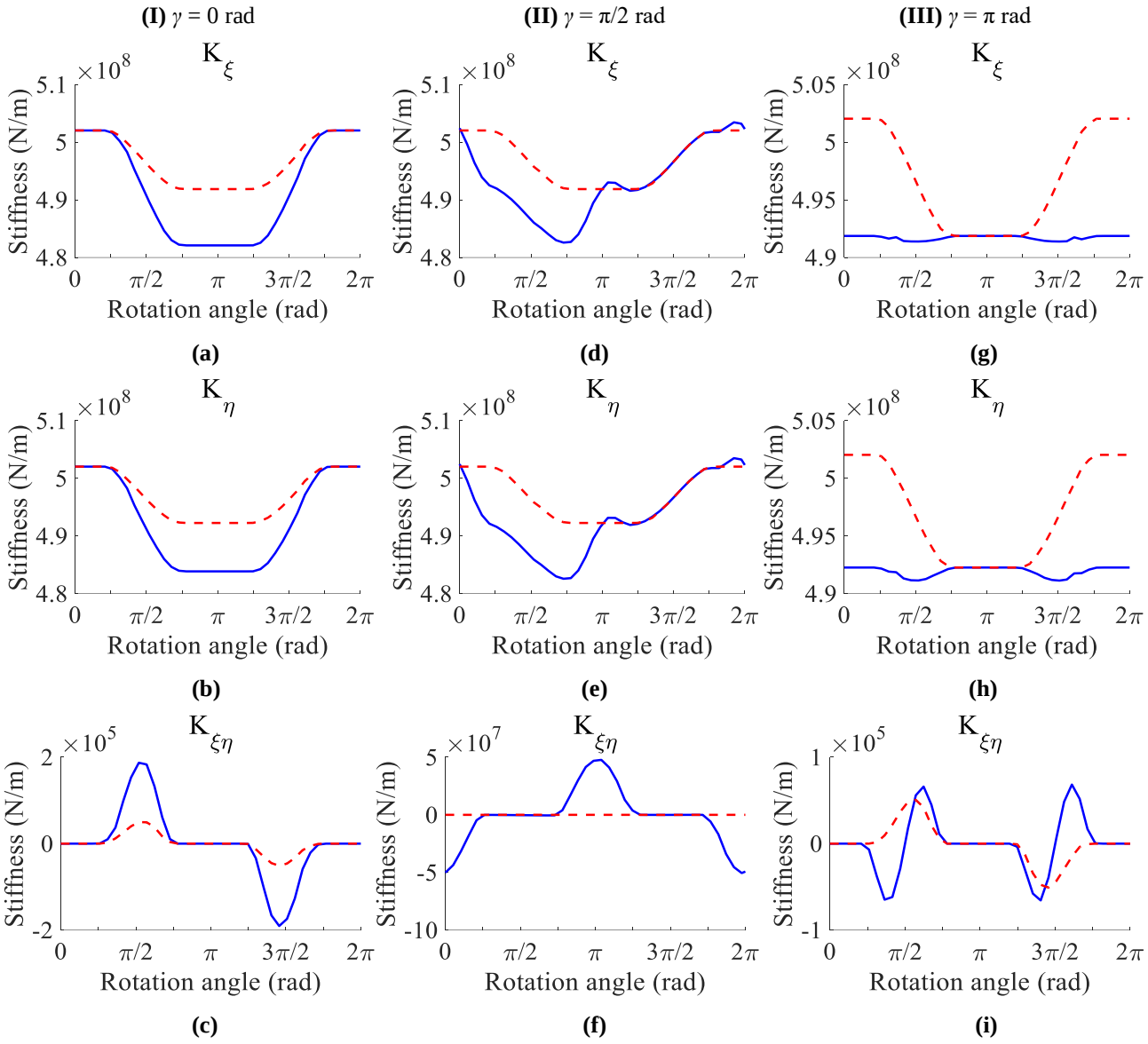

Fig. 3 Stiffness variations with rotation angles under $1/2\Omega_0$, **I** γ = 0 rad: **a** direct stiffness in ξ direction, **b** direct stiffness in η direction, **c** cross-coupled stiffness; **II** $\gamma = \pi/2$ rad: **d** direct stiffness in ξ direction, **e** direct stiffness in η direction, **f** cross-coupled stiffness; **III** $\gamma = \pi$ rad: **g** direct stiffness in ξ direction, **h** direct stiffness in η direction, **i** cross-coupled stiffness. ——— coupled rotor, — — uncoupled rotor

3.1 Stiffness variation with rotation angles

Figure 3 describes the variations of direct stiffness (K_ξ and K_η) and cross-coupled stiffness ($K_{\xi\eta}$) with rotation angles of the coupled and uncoupled rotors under $1/2\Omega_0$, with an assumption of crack-1 is fully closed when the rotation angle $\theta = 0$ and fully open as $\theta = \pi$ rad.

When the crack orientation angle γ is 0, K_ξ and K_η in Figs. 3(a)-(b) indicate that the two cracks start to open as θ is about $\pi/4$ rad, stay fully open in the range of $\theta = 3\pi/4$ - $5\pi/4$ rad, and then turn to close. $K_{\xi\eta}$ reaches a maximum and a minimum value when θ is approximately

π/2 rad and 3π/2 rad, and it is 0 in the remaining state, shown in Fig. 3(c). The two cracks remain open or closed simultaneously, so there is only a single crack breathing phenomenon in one rotation cycle, which is in accordance with the results of a two-crack Jeffcott rotor in Ref. [18]. Moreover, the stiffness variation with rotation angles of the coupled and uncoupled rotors shows that the systemic stiffness of coupled rotor decreases and increases dramatically while θ = π/4 - 3π/4 rad and θ = 5π/4 - 7π/4 rad, respectively, because of the coupling effect between cracks.

As γ changes to π/2 rad, the direct stiffness K_ξ and K_η of the coupled rotor achieve a minimum value at θ = 3π/4 rad because the two cracks are fully open, shown in Figs. 3(d)-(e). K_ξ and K_η begin to increase gradually, and then reach a local minimum at θ = 5π/4 rad, because crack-1 closes completely and crack-2 opens fully at this angle. From Fig. 3(f), $K_{\xi\eta}$ of the coupled rotor reaches a maximum value as θ equals approximately π rad and a minimum value as θ is about 2π rad. For the uncoupled rotor, the variations of K_ξ and K_η are similar as those at γ = 0, while its $K_{\xi\eta}$ remains zero in a rotation period.

When the two cracks are opposite to each other with γ = π rad, the breathing of two cracks is always in the opposite trend, which is why there are two similar changes in direct and cross-coupled stiffness of the coupled rotor during one rotation cycle in Figs. 3(g)-(i). It is impossible for the two opposite cracks to be fully open or closed at the same time, inducing slight changes of K_ξ and K_η for the coupled rotor. The stiffness variations of the uncoupled rotor resemble those when γ = 0, which cannot reflect the actual breathing of the two cracks at γ = π rad.

Figure 3 proves that the nonlinear stiffness variation of the coupled rotor model is different from that of the uncoupled rotor model due to the coupling effect between cracks in the coupled rotor model. The great differences between the stiffness variations of the two kinds of rotor models indicate that the coupled rotor model should be used to represent the inherent nonlinear dynamic behaviors of a multi-crack rotor system.

3.2 Effects of crack orientation angles

The variations of harmonic components and orbits with crack orientation angles (γ = 0, π/2, π rad) at the 21st node for the coupled and uncoupled rotors are investigated as unbalance orientation angle β = 0, shown in Figs. 4-5.

Figure 4 indicates that the crack orientation angle seriously affects the harmonic component amplitudes, especially for the coupled rotor. Most of 1X amplitudes of the coupled rotor are larger than those of the uncoupled rotor. For super-harmonic components, the amplitudes of 2X (when γ = 0 and π rad) and 3X (as γ = 0 and π/2 rad) of the coupled rotor are significantly greater than those of the uncoupled rotor. There is almost no 2X when γ = π/2 rad and no 3X as γ = π rad for

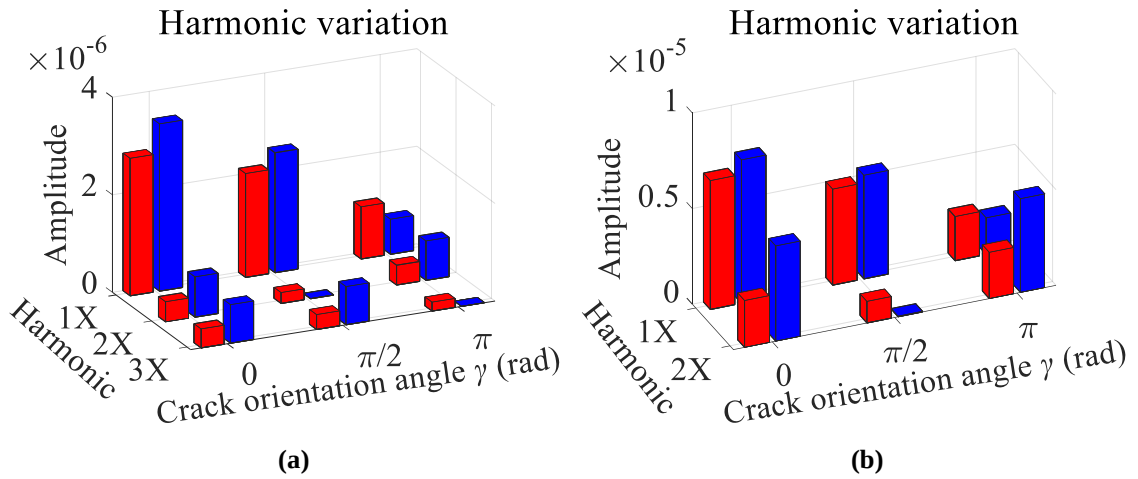

Fig. 4 Amplitude variations of harmonic components with crack orientation angles: **a** $1/3\Omega_0$, **b** $1/2\Omega_0$. coupled rotor, uncoupled rotor

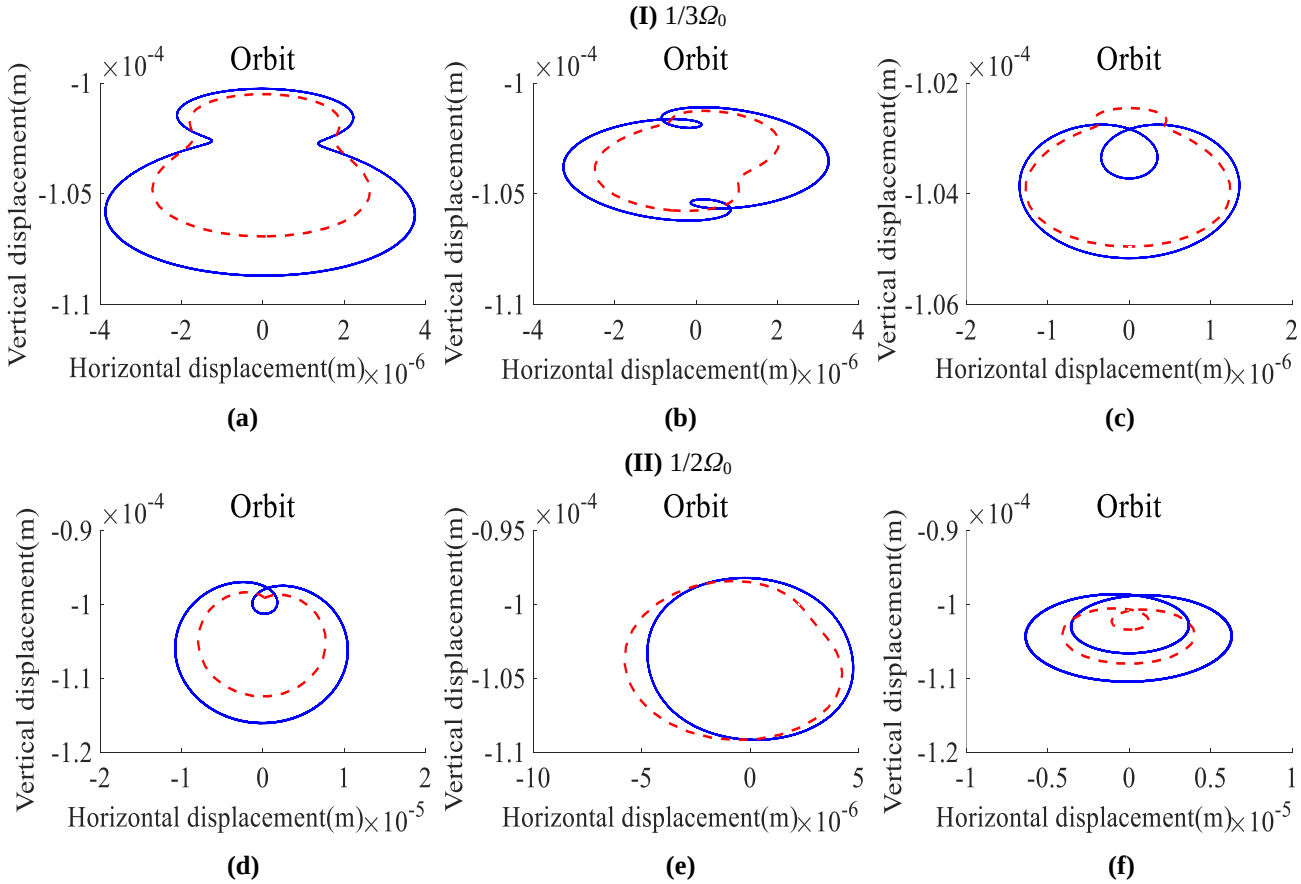

Fig. 5 Orbits with crack orientation angles, **I** $1/3\Omega_0$: **a** $\gamma = 0$, **b** $\gamma = \pi/2$ rad, **c** $\gamma = \pi$ rad; **II** $1/2\Omega_0$: **d** $\gamma = 0$, **e** $\gamma = \pi/2$ rad, **f** $\gamma = \pi$ rad. coupled rotor, uncoupled rotor

the coupled rotor. When γ changes from 0 to π rad, both the 1X and 3X amplitudes of the coupled and uncoupled rotors decrease gradually, the 2X amplitudes decrease first and then increase for these two rotor models. This is because the two cracks change from

synchronous breathing to asynchronous breathing, and then to opposite breathing in one rotation cycle, demonstrating a good degree of agreement with the stiffness variations in previous section.

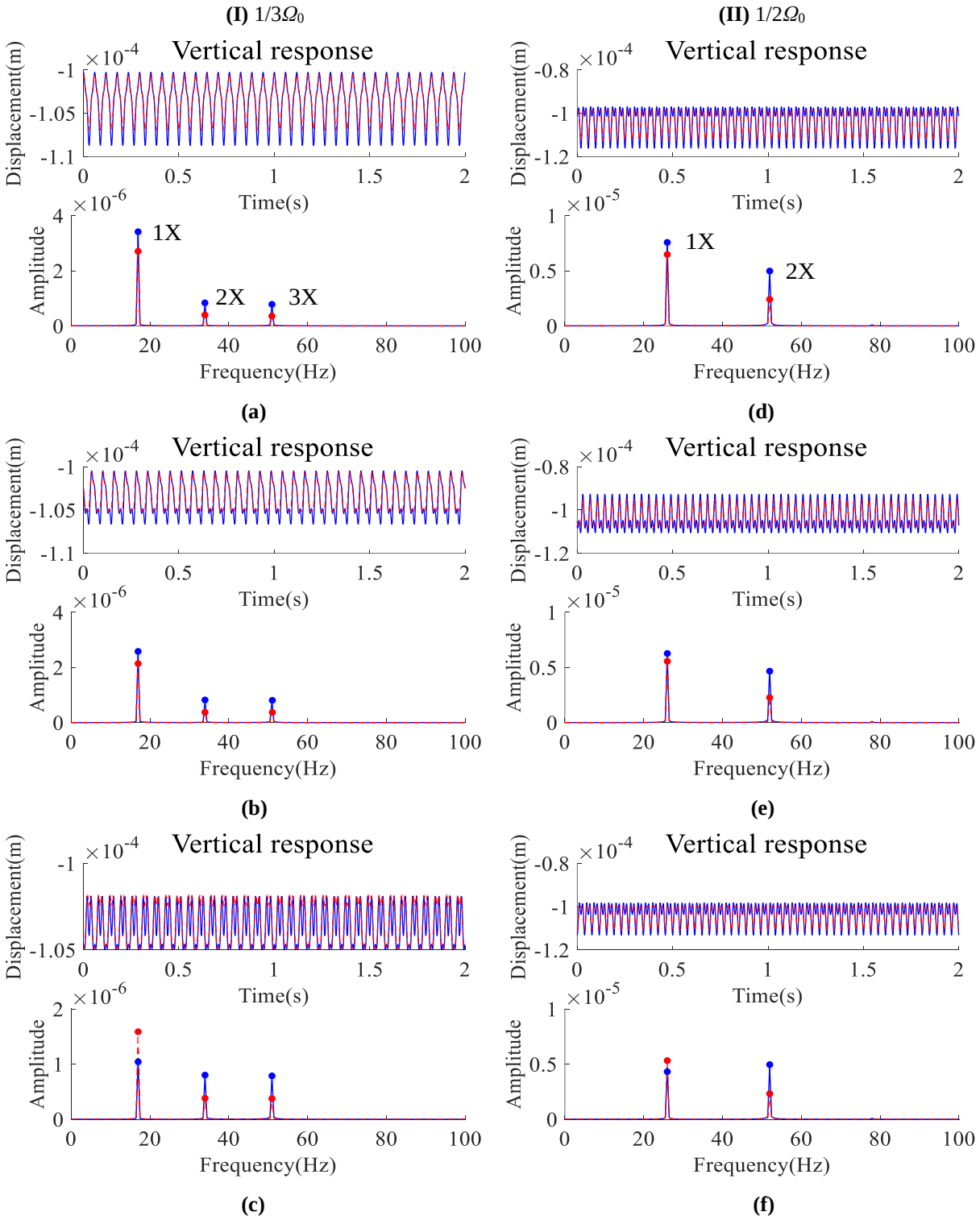

Fig. 6 Vertical responses with unbalance orientation angles, **I** $1/3\Omega_0$: **a** $\beta = 0$, **b** $\beta = \pi/2$ rad, **c** $\beta = \pi$ rad; **II** $1/2\Omega_0$: **d** $\beta = 0$, **e** $\beta = \pi/2$ rad, **f** $\beta = \pi$ rad. ——— coupled rotor — — — uncoupled rotor

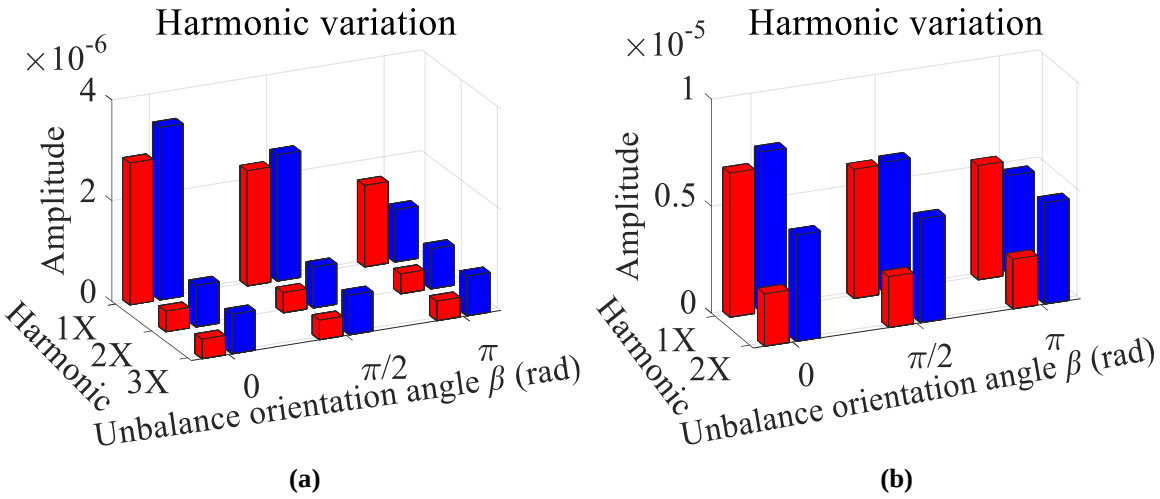

Fig. 7 Amplitude variations of harmonic components with unbalance orientation angles: **a** $1/3\Omega_0$, **b** $1/2\Omega_0$. coupled rotor, uncoupled rotor

The orbit plots can intuitively reflect the systemic nonlinear characteristics, which are widely used for pathological detection in industrial and medical studies [19, 33-38]. Here, the rotor orbits with different crack orientation angles at $1/3\Omega_0$ and $1/2\Omega_0$ are depicted in Fig. 5. It is clear that most of axis orbits of the coupled rotor are slightly larger than those of the uncoupled rotor, resulting from the increased nonlinear flexibility by the coupling effect between cracks, in which the orbits of the coupled rotor with $\gamma = 0$ are well consistent with the results of a rotor with a crack of 1.6 mm depth in Ref. [39]. Furthermore, the shape and number of the concavities and inner loops can be used as important indicators of the presence of rotor cracks.

3.3 Effects of unbalance orientation angles

Figure 6 shows the vertical responses of the coupled and uncoupled rotors while unbalance orientation angle $\beta = 0, \pi/2, \pi$ rad and $\gamma = 0$. It can be found that the displacements of the coupled rotor are larger than those of the uncoupled rotor in time domain responses. And the 2X and 3X amplitudes of the coupled rotor are nearly twice as those of the uncoupled rotor.

Figure 7 shows the amplitude variations of harmonic components with unbalance orientation angle. The 1X amplitudes decrease gradually and the 2X and 3X amplitudes change slightly for the two rotor models with β changes from 0 to π rad. This is because the unbalance force mainly excites 1X component, and the increase in unbalance orientation angle suppresses the magnitude of 1X component [40]. Therefore, the super-harmonic components in the multi-crack rotor response are basically not affected by the unbalance orientation angle.

Figure 8 shows the orbits when $\beta = 0, \pi/2, \pi$ rad at the speed of $1/3\Omega_0$ and $1/2\Omega_0$. The orbits

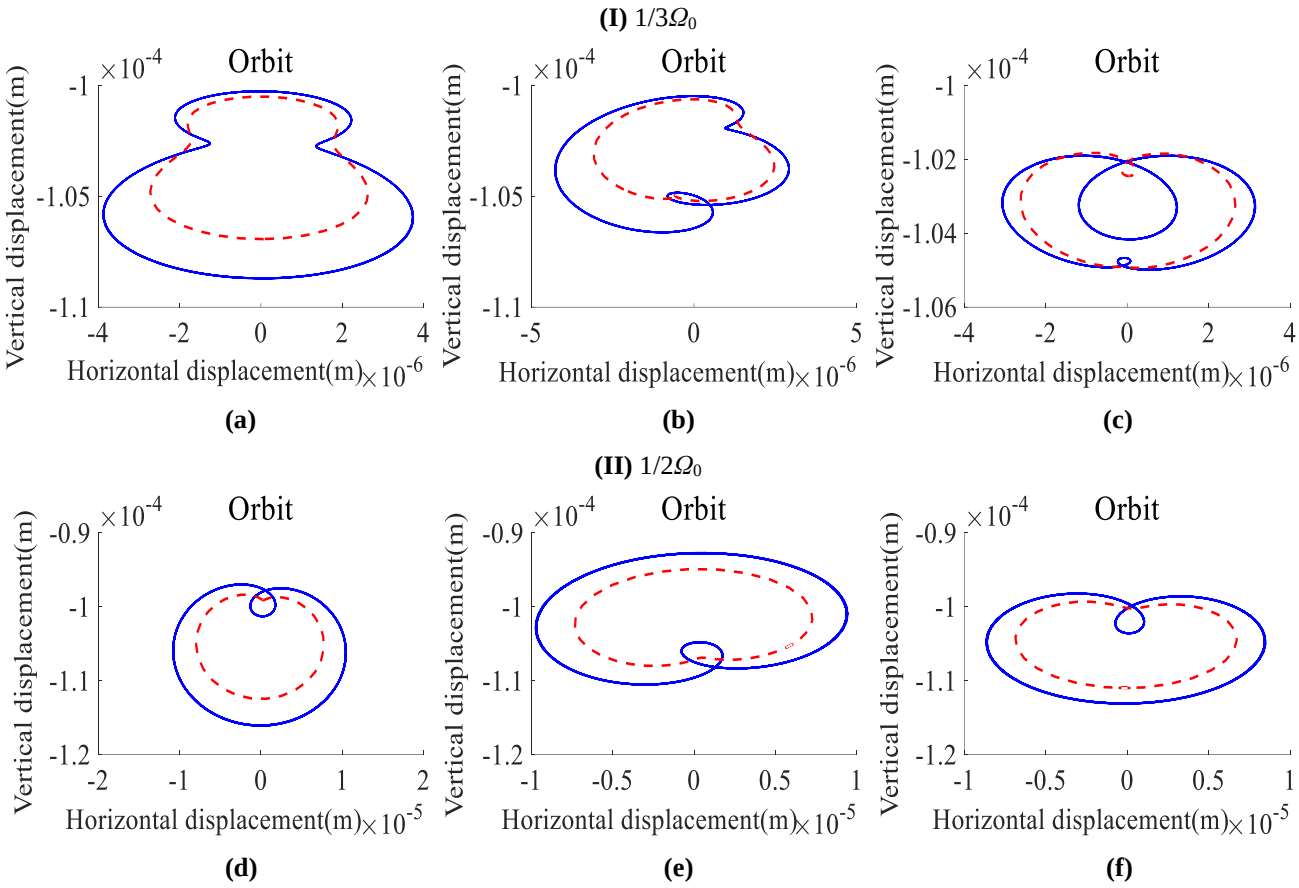

Fig. 8 Orbits with unbalance orientation angles, **I** $1/3\Omega_0$: **a** $\beta = 0$, **b** $\beta = \pi/2$ rad, **c** $\beta = \pi$ rad; **II** $1/2\Omega_0$: **d** $\beta = 0$, **e** $\beta = \pi/2$ rad, **f** $\beta = \pi$ rad. ——— coupled rotor, — — — uncoupled rotor

of the coupled rotor are slightly bigger than those of the uncoupled rotor due to the increased flexibility induced by the coupling effect between cracks.

It can be concluded that the complex morphological features of orbits of the coupled rotor can be confidently attributed to the severe nonlinear change of the systemic stiffness. The multi-crack coupling effect has a prominent influence on the rotor nonlinear dynamic characteristics, and cannot be neglected in the FE modelling of a multi-crack rotor.

3.4 Effects of crack depths

In this subsection, the effects of crack depths on the rotor dynamic characteristics are investigated with crack orientation angle $\gamma = 0$ and unbalance orientation angle $\beta = 0$. The amplitudes of harmonic components in vertical response for the coupled and uncoupled rotors with seven different crack depth combinations at the speed of $1/3\Omega_0$ and $1/2\Omega_0$ are tabulated in Tables 2-3. To further illustrate the influences of crack depth, the super-harmonic amplitudes of the two multi-crack rotors are mapped in Fig. 9, in which Fig. 9(b) is a partially enlarged view

Table 2 Harmonic amplitudes with crack depths at $1/3\Omega_0$

Case	Crack depth		Harmonic component					
			1X		2X		3X	
	crack-1	crack-2	coupled	uncoupled	coupled	uncoupled	coupled	uncoupled
1	0.05*D*	0.05*D*	2.45×10^{-6}	2.43×10^{-6}	3.62×10^{-8}	1.85×10^{-8}	4.55×10^{-8}	2.26×10^{-8}
2	0.05*D*	0.1*D*	2.55×10^{-6}	2.50×10^{-6}	1.07×10^{-7}	7.30×10^{-8}	1.22×10^{-7}	7.79×10^{-8}
3	0.1*D*	0.1*D*	2.64×10^{-6}	2.52×10^{-6}	1.79×10^{-7}	8.95×10^{-8}	1.99×10^{-7}	9.89×10^{-8}
4	0.1*D*	0.15*D*	2.83×10^{-6}	2.67×10^{-6}	3.09×10^{-7}	1.90×10^{-7}	3.32×10^{-7}	1.95×10^{-7}
5	0.15*D*	0.15*D*	3.02×10^{-6}	2.71×10^{-6}	4.40×10^{-7}	2.20×10^{-7}	4.66×10^{-7}	2.32×10^{-7}
6	0.15*D*	0.2*D*	3.32×10^{-6}	2.95×10^{-6}	6.27×10^{-7}	3.63×10^{-7}	6.12×10^{-7}	3.36×10^{-7}
7	0.2*D*	0.2*D*	3.43×10^{-6}	2.82×10^{-6}	8.27×10^{-7}	4.13×10^{-7}	7.91×10^{-7}	3.90×10^{-7}

Table 3 Harmonic amplitudes with crack depths at $1/2\Omega_0$

Case	Crack depth		Harmonic component			
			1X		2X	
	crack-1	crack-2	coupled	uncoupled	coupled	uncoupled
1	0.05*D*	0.05*D*	6.57×10^{-6}	6.55×10^{-6}	2.05×10^{-7}	1.03×10^{-7}
2	0.05*D*	0.1*D*	6.69×10^{-6}	6.64×10^{-6}	6.08×10^{-7}	3.93×10^{-7}
3	0.1*D*	0.1*D*	6.80×10^{-6}	6.66×10^{-6}	1.01×10^{-6}	5.06×10^{-7}
4	0.1*D*	0.15*D*	7.03×10^{-6}	6.84×10^{-6}	1.78×10^{-6}	1.05×10^{-6}
5	0.15*D*	0.15*D*	7.26×10^{-6}	6.89×10^{-6}	2.54×10^{-6}	1.26×10^{-6}
6	0.15*D*	0.2*D*	7.63×10^{-6}	7.18×10^{-6}	3.64×10^{-6}	2.04×10^{-6}
7	0.2*D*	0.2*D*	7.50×10^{-6}	6.74×10^{-6}	4.98×10^{-6}	2.45×10^{-6}

of the first three cases in Fig. 9(a), and so is true for Figs. 9(c)-(d).

It can be seen from Tables 2-3 and Fig. 9 that the response amplitudes increase with the increment of crack depth. The 1X amplitude of the coupled rotor is slightly larger than that of the uncoupled rotor at a same crack depth, while the 2X and 3X amplitudes of the coupled rotor are nearly twice as those of the uncoupled rotor. Therefore, the magnitudes of super-harmonic components of the coupled rotor are more sensitive to the crack depth variation compared to those of the uncoupled rotor.

The weak super-harmonic components induced by early cracks are easily submerged in system responses, which brings significant challenges to dynamic analysis and fault diagnosis of rotor systems. For the small crack depths in the first three cases, it can be found from Tables 2-3 and Figs. 9(b) and (d) that the amplitudes of most of 2X and 3X components of the coupled rotor are nearly twice as those of the uncoupled rotor, which clearly shows that the prominent super-harmonic components in dynamic responses of the coupled rotor can represent the faint fault features of slight crack.

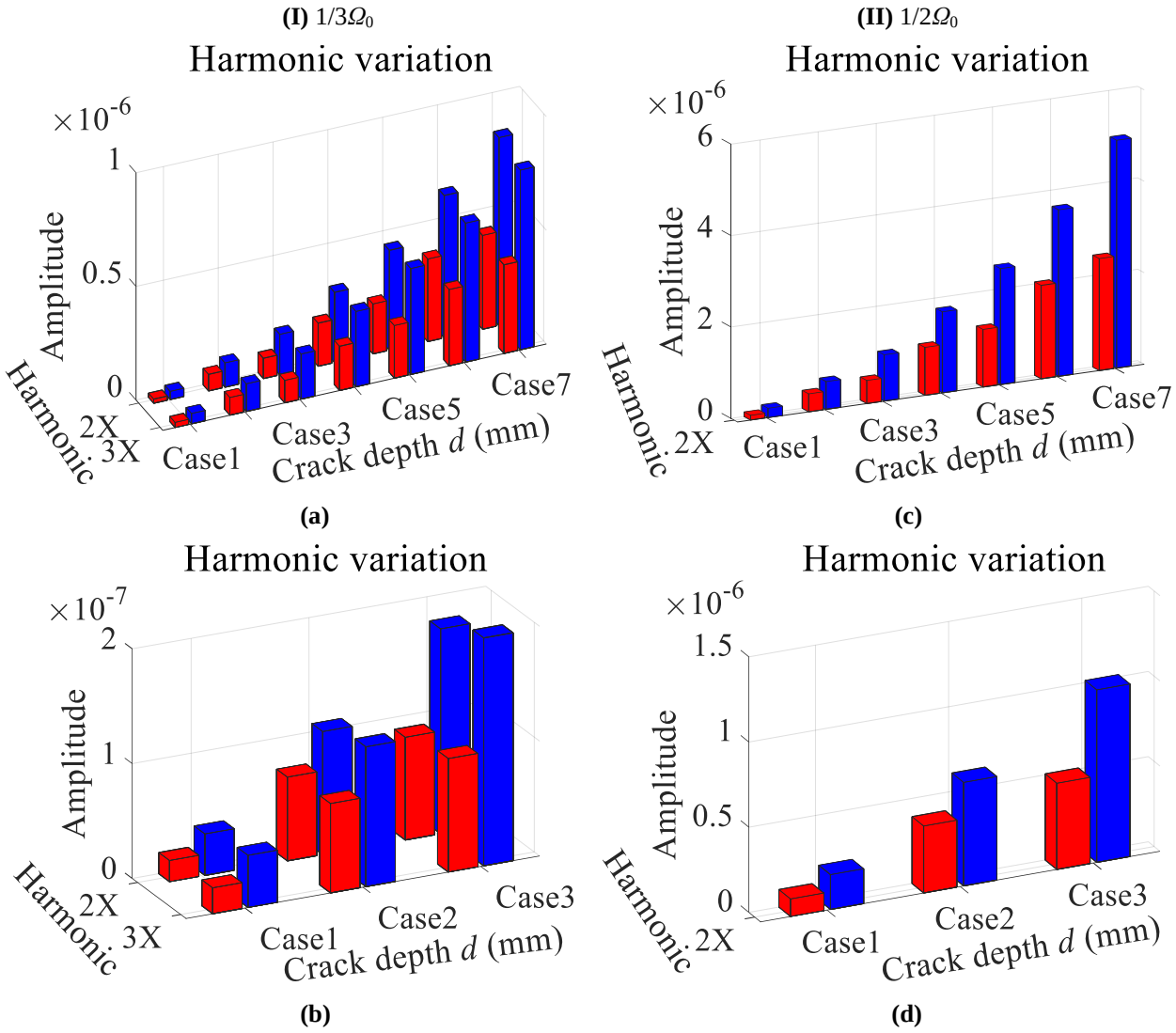

Fig. 9 Super-harmonic amplitudes with crack depths, **I** $1/3\Omega_0$: **a** seven cases, **b** partially enlarged view of first three cases; **II** $1/2\Omega_0$: **c** seven cases, **d** partially enlarged view of first three cases. coupled rotor, uncoupled rotor

Therefore, the coupled rotor model provides a promising application for early crack detection of cracked rotor systems.

4 Experimental investigation

The orbit shapes of the coupled rotor model at $1/2\Omega_0$ in Figs. 5 and 8 are consistent with the results of a Jeffcott rotor with two cracks in Ref. [18]. In order to further validate the proposed model, the vibration signals with different crack orientation angles and unbalance orientation angles are collected on an experimental bench. The sampling frequency is 5000 Hz, the measuring points are located at the 21st and 31st nodes of the rotating shaft, and the rotational speeds are $1/3\Omega'_0$ and $1/2\Omega'_0$ (Ω'_0 is the first critical speed of the experimental bench, Ω'_0 = 3296 rpm). For an uncracked rotor, all experimental orbits in the

1/3 and 1/2 subcritical speed zones are of an approximate ellipse shape [41].

4.1 Experimental setup

The experimental bench includes six parts: a servo motor, three two-crack shafts with different crack orientation angles, two discs, two ball bearings, a flexible coupling, and four eddy current displacement sensors, as shown in Fig. 10. The length and diameter of shafts are 0.6 m and 0.01 m, respectively. Two slits with a same depth of 0.002 m are obtained by wire cutting to simulate the breathing cracks, which are located at 0.25 m and 0.35 m away from the left end of shafts. The eddy current displacement sensors at the same measuring points are perpendicular to each other on a sensor frame. The parameters of the experimental bench components are displayed in Table 4.

4.2 Results and discussions

Figure 11 illustrates the experimental orbits when crack orientation angle $\gamma = 0, \pi/2, \pi$ rad and unbalance orientation angle $\beta = 0$. Figure 11(a) shows that the orbit includes two concavities, agreeing with the orbit of a rotor with a crack of 3.2 mm depth in Ref. [41]. The orbit in Fig. 11(b) has two inner loops, while the ones in Figs. 11(c)-(d) and (f) contain only an inner loop, the one in Fig. 11(e) looks like an ellipse. The morphological features of orbits with different crack orientation angles agree well with the simulated results of the coupled rotor model in Fig. 5.

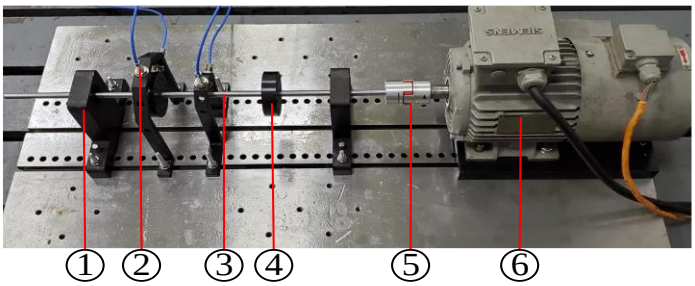

Fig. 10 Description of experimental bench: ① bearing, ② eddy current displacement sensor, ③ multi-crack shaft, ④ disc, ⑤ flexible coupling, ⑥ servo motor

Table 4 Parameters of experimental bench

Part	Type	Quantity
Servo motor	SIEMENSE G90A IP55	1
Multi-crack shaft	40Cr	3
Disc	45# steel	2
Bearing	SKF-6300	2
Flexible coupling	LM-45-10-24	1
Eddy current displacement sensor	ZA21-0803	4

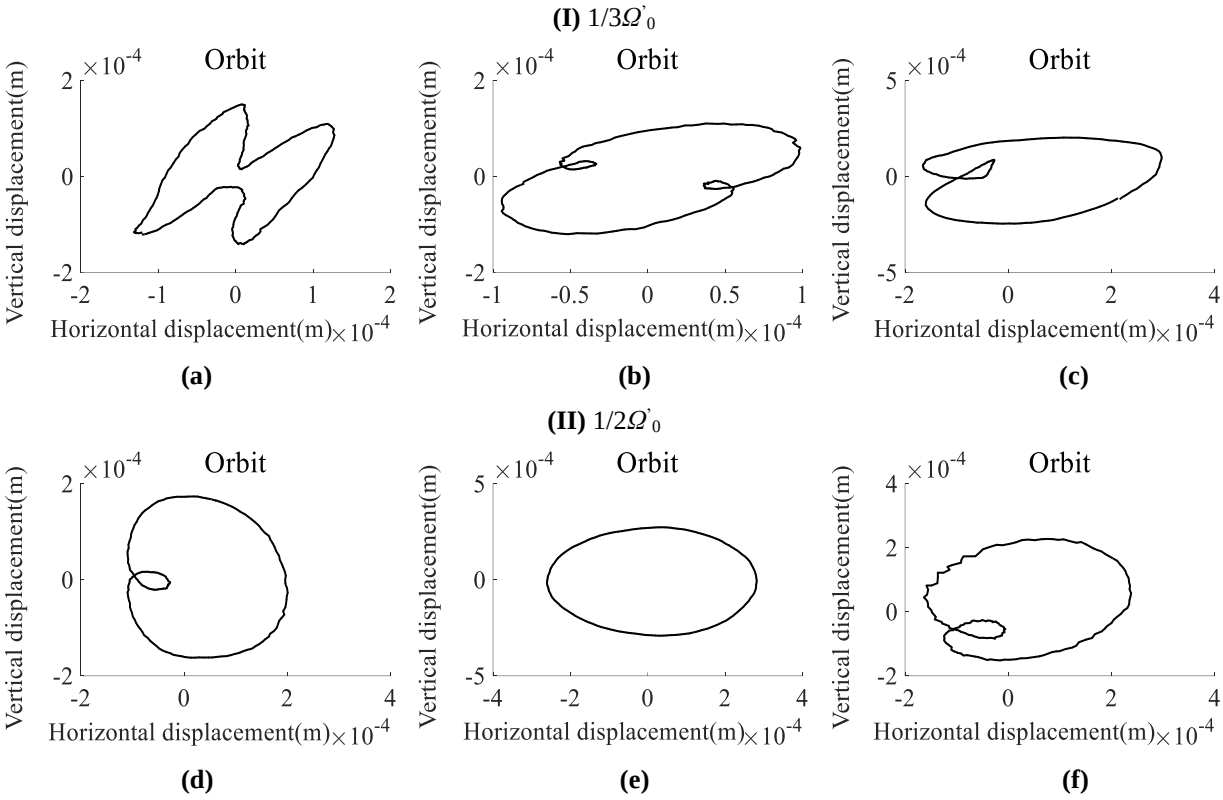

Fig. 11 Experimental orbits with crack orientation angles, **I** $1/3\Omega'_0$: **a** $\gamma = 0$, **b** $\gamma = \pi/2$ rad, **c** $\gamma = \pi$ rad; **II** $1/2\Omega'_0$: **d** $\gamma = 0$, **e** $\gamma = \pi/2$ rad, **f** $\gamma = \pi$ rad

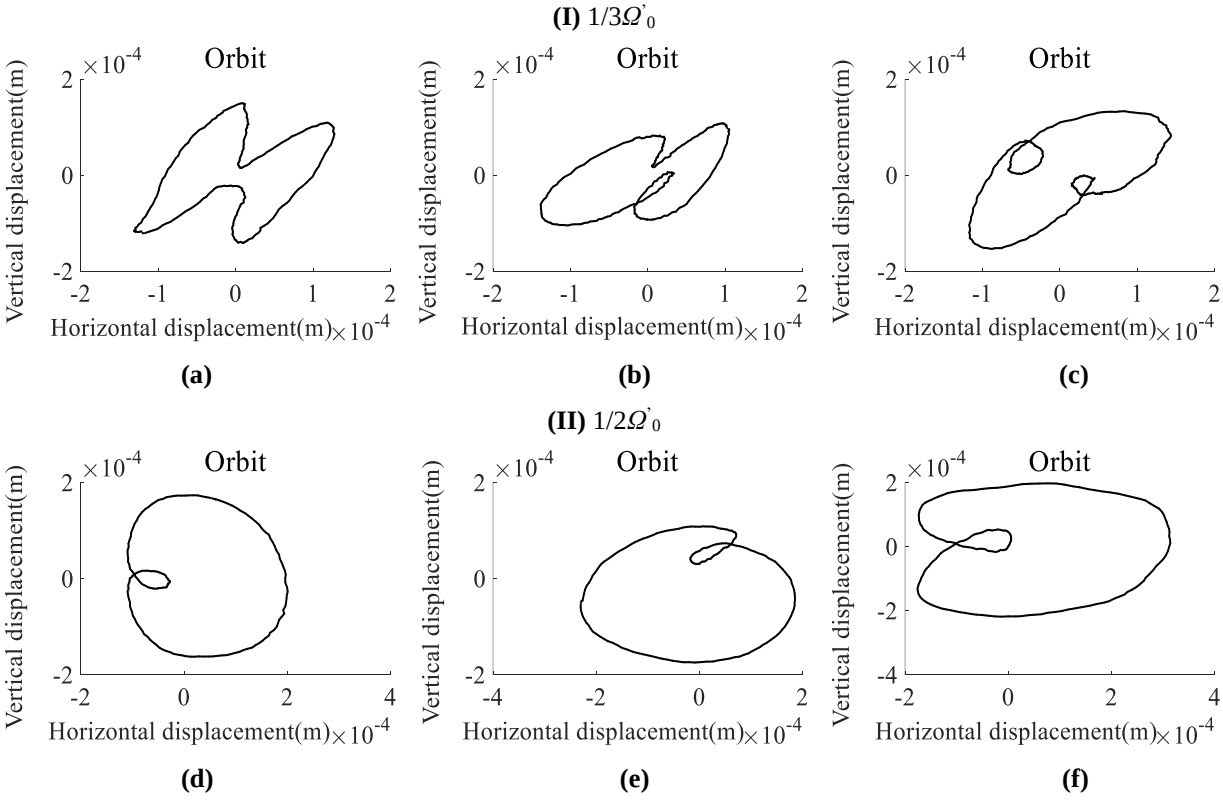

Fig. 12 Experimental orbits with unbalance orientation angles, **I** $1/3\Omega'_0$: **a** $\beta = 0$, **b** $\beta = \pi/2$ rad, **c** $\beta = \pi$ rad; **II** $1/2\Omega'_0$: **d** $\beta = 0$, e $\beta = \pi/2$ rad, **f** $\beta = \pi$ rad

Figure 12 displays the orbits when $\beta = 0$, π/2, π rad and $\gamma = 0$. The orbit of Fig. 12(b) contains a concavity and an inner loop, and the one in Fig. 12(c) has two inner loops of different sizes, coinciding with the results of the coupled rotor model in Figs. 8(b)-(c). It can also be seen from Figs. 12(d)-(f) and Figs. 8(d)-(f) that the shape and phase change of the experimental and simulated orbits are similar.

Several rotor vibration responses with $\beta = 0$, π/2, π rad and $\gamma = 0$ at the speed of $1/2\Omega'_0$ are shown in Fig. 13. It can be seen that the ratios of the super-harmonic amplitudes to the fundamental harmonic amplitudes are in good agreement with those of the coupled rotor model in Figs. 6(d)-(f). These obvious super-harmonic amplitudes can be extracted as the feature for crack diagnosis of rotors, even for early-stage crack detection.

The experimental morphological features of rotor orbits (Figs. 11-12) are generally consistent with the simulated ones of the coupled rotor model in Figs. 5 and 8. The relative proportions of harmonic amplitudes are also in accordance with those of the coupled rotor model. The excellent agreement between the theoretical and experimental findings demonstrates the correctness of the coupled multi-crack rotor model, which also proves that the coupling effect between cracks is really existent and cannot be ignored in actual rotors.

It is worth noting that there is a π/2-rad phase difference between the simulated orbits and experimental ones, which is attributed to

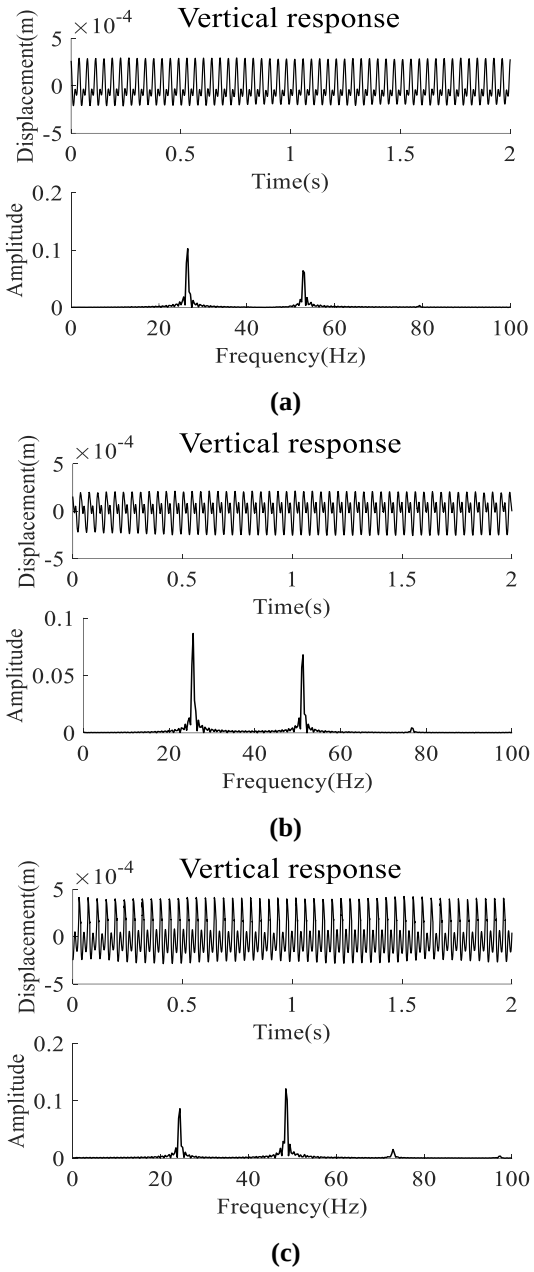

Fig. 13 Experimental responses with $\gamma = 0$ at $1/2\Omega'_0$: **a** $\beta = 0$, **b** $\beta = \pi/2$ rad, **c** $\beta = \pi$ rad

the relative angle of two eddy current displacement sensors is less than π/2 rad resulted from the machining error of the sensor frames [42]. Additionally, there are some undesirable small disturbances in experimental orbits and spectrums due to the rotation speed fluctuation of servo motor and measurement noise.

5 Conclusions

This paper proposes a coupled multi-crack rotor model by considering the coupling effect between cracks under complex excitations as additional flexibility. The rotor dynamic responses with different crack orientation angles, unbalance orientation angles and crack depths are analysed at 1/3 and 1/2 subcritical speeds. The specific conclusions are summarised as follows:

(1) The proposed coupled multi-crack rotor model gives a detailed description of the coupling mechanism between cracks under complex excitations including bending moments, torques and so on.

(2) Compared with the uncoupled rotor model ignoring the interaction between cracks, the coupled rotor model can more accurately represent the inherent complicated nonlinear dynamic characteristics of actual cracked rotors.

(3) The majority of the vibration responses (including the orbits) of the coupled rotor model are larger than those of the uncoupled rotor model due to the increased nonlinear flexibility caused by the coupling effect between cracks. The magnitudes of most of 2X and 3X components of the coupled rotor are nearly twice as those of the uncoupled rotor. The prominent super-harmonic components and morphological characteristics of orbits can be used for early crack detection and crack parameter identification in rotors.

(4) The good consistency between the experimental and simulated results confirms the correctness and feasibility of the developed coupled rotor model for the crack detection in practice.

This work is of great significance to the dynamic characteristics research and early crack detection for multi-crack rotor systems in practical engineering, which is expected to be helpful for the quantitative identification of multi-crack parameters in rotors. Moreover, based on the above theoretical research and experimental bench, this study can provide a large amount of data in various working conditions for applications of the signal-based and artificial intelligence-based methods in rotor fault diagnosis. However, this paper only analyses the nonlinear dynamic behavior of rotor systems at stable subcritical speeds, without considering the effects of speed variations (especially under start-up and shut-down conditions) and the noise interference, which will be the focus and challenge of future work.

Acknowledgements This work was supported by the National Natural Science Foundation of China (No. 51875482).

Compliance with ethical standards

Conflict of interest The authors declare that there are no any associative competing interests regarding the work submitted.

CRediT authorship contribution statement Conceptualisation, Methodology: Libo Xiong, Chunrong Hua and Dawei Dong; Validation, Formal analysis, Software, Investigation: Libo Xiong and Lumei Lv; Writing-original draft preparation: Libo Xiong and Chunrong Hua; Writing-review and editing: Chunrong Hua and Huajiang Ouyang; Funding acquisition: Dawei Dong; Data curation, Resources: Chunrong Hua and Dawei Dong; Supervision: Dawei Dong and Huajiang Ouyang.

Data Availability Statement The datasets generated during and/or analysed during the current study are not publicly available due to the confidentiality requirements of the project but are available from the corresponding author on reasonable request.

Appendix A: Additional displacements

$$
\begin{aligned}
u_1^{1\,\mathrm{c}} = {} & \frac{2}{E'\pi R^4}\iint_{A^{1\,\mathrm{c}}}(\sin^4\theta F_1^2 + m_s\sin^2\theta\cos^2\theta F_{\mathrm{III}}^2)\alpha \mathrm{d}A^{\mathrm{c}}\bullet P_1^{2\,\mathrm{c}} \\
& + \frac{1}{E'\pi R^6}\iint_{A^{1\,\mathrm{c}}}(4x_s h\sin^4\theta F_1F_2 + 4m_s x_s h\sin^2\theta\cos^2\theta F_{\mathrm{III}}^2)\alpha \mathrm{d}A^{\mathrm{c}}\bullet(P_2^{2\,\mathrm{c}}\cos\gamma - P_3^{2\,\mathrm{c}}\sin\gamma) \\
& + \frac{1}{E'\pi R^6}\iint_{A^{1\,\mathrm{c}}}\begin{pmatrix} 2kR^2\sin 2\theta\sin^2\theta F_1^2 + 2kR^2\sin\theta\cos\theta\cos 2\theta F_{\mathrm{III}}^2 \\ +8x_s w\sin^5\theta F_1^2 + 8x_s m_s w\sin^3\theta\cos^2\theta F_{\mathrm{III}}^2 \end{pmatrix}\alpha \mathrm{d}A^{\mathrm{c}}\bullet(P_2^{2\,\mathrm{c}}\sin\gamma + P_3^{2\,\mathrm{c}}\cos\gamma) \\
& + \frac{1}{E'\pi R^6}\iint_{A^{1\,\mathrm{c}}}(2h\sin 2\theta\sin^2\theta F_1F_2 + 2m_s h\sin\theta\cos\theta\cos 2\theta F_{\mathrm{III}}^2)\alpha \mathrm{d}A^{\mathrm{c}}\bullet P_4^{2\,\mathrm{c}} \\
& + \frac{2}{E'\pi R^6}\iint_{A^{1\,\mathrm{c}}}(8w\sin^5\theta F_1^2 + 8m_s w\cos^2\theta\sin^3\theta F_{\mathrm{III}}^2)\alpha \mathrm{d}A^{\mathrm{c}}\bullet(P_5^{2\,\mathrm{c}}\cos\gamma - P_6^{2\,\mathrm{c}}\sin\gamma) \\
& + \frac{-1}{E'\pi R^6}\iint_{A^{1\,\mathrm{c}}}(4h\sin^4\theta F_1F_2 + 4m_s h\sin^2\theta\cos^2\theta F_{\mathrm{III}}^2)\alpha \mathrm{d}A^{\mathrm{c}}\bullet(P_5^{2\,\mathrm{c}}\sin\gamma + P_6^{2\,\mathrm{c}}\cos\gamma)
\end{aligned}
\tag{A.1}
$$

$$
\begin{aligned}
u_2^{1\,\mathrm{c}} = {} & \frac{2}{E'\pi R^8}\iint_{A^{1\,\mathrm{c}}}(4x_s^2h^2\sin^4\theta F_2^2 + 4m_s x_s^2h^2\sin^2\theta\cos^2\theta F_{\mathrm{III}}^2 + k^2R^4\sin^2\theta F_{\mathrm{II}}^2)\alpha \mathrm{d}A^{\mathrm{c}}\bullet(P_2^{2\,\mathrm{c}}\cos\gamma - P_3^{2\,\mathrm{c}}\sin\gamma) \\
& + \frac{1}{E'\pi R^8}\iint_{A^{1\,\mathrm{c}}}\begin{pmatrix} 4x_s khR^2\sin 2\theta\sin^2\theta F_2^2 + 4x_s m_s khR^2\sin\theta\cos\theta\cos 2\theta F_{\mathrm{III}}^2 \\ +16hwx_s^2\sin^5\theta F_1F_2 + 16m_s hwx_s^2\sin^3\theta\cos^2\theta F_{\mathrm{III}}^2 \end{pmatrix}\alpha \mathrm{d}A^{\mathrm{c}}\bullet(P_2^{2\,\mathrm{c}}\sin\gamma + P_3^{2\,\mathrm{c}}\cos\gamma) \\
& + \frac{1}{E'\pi R^8}\iint_{A^{1\,\mathrm{c}}}\begin{pmatrix} 4x_s h^2\sin 2\theta\sin^2\theta F_2^2 + 4x_s m_s h^2\sin\theta\cos\theta\cos 2\theta F_{\mathrm{III}}^2 \\ +4kwR^2\sin^3\theta F_{\mathrm{II}}^2 \end{pmatrix}\alpha \mathrm{d}A^{\mathrm{c}}\bullet P_4^{2\,\mathrm{c}} \\
& + \frac{1}{E'\pi R^8}\iint_{A^{1\,\mathrm{c}}}(16x_s hw\sin^5\theta F_1F_2 + 16x_s m_s hw\cos^2\theta\sin^3\theta F_{\mathrm{III}}^2)\alpha \mathrm{d}A^{\mathrm{c}}\bullet(P_5^{2\,\mathrm{c}}\cos\gamma - P_6^{2\,\mathrm{c}}\sin\gamma) \\
& + \frac{-2}{E'\pi R^8}\iint_{A^{1\,\mathrm{c}}}(4x_s h^2\sin^4\theta F_2^2 + 4x_s m_s h^2\sin^2\theta\cos^2\theta F_{\mathrm{III}}^2)\alpha \mathrm{d}A^{\mathrm{c}}\bullet(P_5^{2\,\mathrm{c}}\sin\gamma + P_6^{2\,\mathrm{c}}\cos\gamma)
\end{aligned}
\tag{A.2}
$$

$$u_3^{1\,c}=\frac{2}{E'\pi R^8}\iint_{A^{1\,c}}\begin{pmatrix}k^2R^4\sin^2\theta F_1^2+m_sk^2R^4\cos^2 2\theta F_{\mathrm{III}}^2+16x_s^2w^2\sin^6\theta F_1^2\\+16m_sx_s^2w^2\cos^2\theta\sin^4\theta F_{\mathrm{III}}^2+8kx_swR^2\sin 2\theta\sin^3\theta F_1^2\\+8kx_swR^2\cos\theta\cos 2\theta\sin^2\theta F_{\mathrm{III}}^2\end{pmatrix}\alpha\mathrm{d}A^{\mathrm{c}}\bullet(P_2^{2\,c}\sin\gamma+P_3^{2\,c}\cos\gamma)$$
$$+\frac{1}{E'\pi R^8}\iint_{A^{1\,c}}\begin{pmatrix}8x_shw\sin 2\theta\sin^2\theta F_1F_2+8x_sm_shw\cos\theta\cos 2\theta\sin^2\theta F_{\mathrm{III}}^2\\+2khR^2\sin^2 2\theta F_1F_2+2m_skhR^2\cos^2 2\theta F_{\mathrm{III}}^2\end{pmatrix}\alpha\mathrm{d}A^{\mathrm{c}}\bullet P_4^{2\,c}$$
$$+\frac{1}{E'\pi R^8}\iint_{A^{1\,c}}\begin{pmatrix}8kwR^2\sin 2\theta\sin^3\theta F_1^2+8m_skwR^2\cos\theta\cos 2\theta\sin^2\theta F_{\mathrm{III}}^2\\+32x_sw^2\sin^6\theta F_1^2+32x_sm_sw^2\cos^2\theta\sin^4\theta F_{\mathrm{III}}^2\end{pmatrix}\alpha\mathrm{d}A^{\mathrm{c}}\bullet(P_5^{2\,c}\cos\gamma-P_6^{2\,c}\sin\gamma)$$
$$+\frac{-1}{E'\pi R^8}\iint_{A^{1\,c}}\begin{pmatrix}4khR^2\sin 2\theta\sin^2\theta F_1F_2+4m_skhR^2\sin\theta\cos\theta\cos 2\theta F_{\mathrm{III}}^2\\+16x_shw\sin^5\theta F_1F_2+16x_sm_shw\sin^3\theta\cos^2\theta F_{\mathrm{III}}^2\end{pmatrix}\alpha\mathrm{d}A^{\mathrm{c}}\bullet(P_5^{2\,c}\sin\gamma+P_6^{2\,c}\cos\gamma)$$

(A.3)

$$u_4^{1\,c}=\frac{2}{E'\pi R^8}\iint_{A^{1\,c}}(h^2\sin^2 2\theta F_2^2+m_sh^2\cos^2 2\theta F_{\mathrm{III}}^2+4w^2\sin^4\theta F_{\mathrm{II}}^2)\alpha\mathrm{d}A^{\mathrm{c}}\bullet P_4^{2\,c}$$
$$+\frac{1}{E'\pi R^8}\iint_{A^{1\,c}}(8hw\sin 2\theta\sin^3\theta F_1F_2+8m_shw\cos\theta\cos 2\theta\sin^2\theta F_{\mathrm{III}}^2)\alpha\mathrm{d}A^{\mathrm{c}}\bullet(P_5^{2\,c}\cos\gamma-P_6^{2\,c}\sin\gamma) \quad (A.4)$$
$$+\frac{-1}{E'\pi R^8}\iint_{A^{1\,c}}(4h^2\sin 2\theta\sin^2\theta F_2^2+4m_sh^2\sin\theta\cos\theta\cos 2\theta F_{\mathrm{III}}^2)\alpha\mathrm{d}A^{\mathrm{c}}\bullet(P_5^{2\,c}\sin\gamma+P_6^{2\,c}\cos\gamma)$$

$$u_5^{1\,c}=\frac{2}{E'\pi R^8}\iint_{A^{1\,c}}(16w^2\sin^6\theta F_1^2+16m_sw^2\cos^2\theta\sin^4\theta F_{\mathrm{III}}^2)\alpha\mathrm{d}A^{\mathrm{c}}\bullet(P_5^{2\,c}\cos\gamma-P_6^{2\,c}\sin\gamma)$$
$$+\frac{-1}{E'\pi R^8}\iint_{A^{1\,c}}(16hw\sin^5\theta F_1F_2+16m_shw\cos^2\theta\sin^3\theta F_{\mathrm{III}}^2)\alpha\mathrm{d}A^{\mathrm{c}}\bullet(P_5^{2\,c}\sin\gamma+P_6^{2\,c}\cos\gamma) \quad (A.5)$$

$$u_6^{1\,c}=\frac{2}{E'\pi R^8}\iint_{A^{1\,c}}(4h^2\sin^4\theta F_2^2+4m_sh^2\sin^2\theta\cos^2\theta F_{\mathrm{III}}^2)\alpha\mathrm{d}A^{\mathrm{c}}\bullet(P_5^{2\,c}\sin\gamma+P_6^{2\,c}\cos\gamma) \quad (A.6)$$

Appendix B: Flexibility coefficients

$$g_{11}^{2\sim 1\,c}=\frac{\partial u_1^{2\sim 1\,c}}{\partial P_1^{2\,c}}$$
$$=\frac{2}{E'\pi R^4}\iint_{A^{1\,c}}(\sin^4\theta F_1^2+m_s\sin^2\theta\cos^2\theta F_{\mathrm{III}}^2)\alpha\mathrm{d}A^{\mathrm{c}} \quad (B.1)$$

$$
\begin{aligned}
g_{22}^{2\sim 1\,\mathrm{c}} &= \frac{\partial u_2^{2\sim 1\,\mathrm{c}}}{\partial P_2^{2\,\mathrm{c}}} \\
&= \frac{2}{E'\pi R^8}\iint_{A^{1\,\mathrm{c}}}(4x_s^2h^2\sin^4\theta F_2^2+4m_sx_s^2h^2\sin^2\theta\cos^2\theta F_{\mathrm{III}}^2+k^2R^4\sin^2\theta F_{\mathrm{II}}^2)\alpha\mathrm{d}A^{\mathrm{c}}\bullet\cos^2\gamma \\
&+ \frac{1}{E'\pi R^8}\iint_{A^{1\,\mathrm{c}}}\begin{pmatrix}4x_skhR^2\sin 2\theta\sin^2\theta F_2^2+4x_sm_skhR^2\sin\theta\cos\theta\cos 2\theta F_{\mathrm{III}}^2\\+16hwx_s^2\sin^5\theta F_1F_2+16m_shwx_s^2\sin^3\theta\cos^2\theta F_{\mathrm{III}}^2\end{pmatrix}\alpha\mathrm{d}A^{\mathrm{c}}\bullet\sin\gamma\cos\gamma \\
&+ \frac{2}{E'\pi R^8}\iint_{A^{1\,\mathrm{c}}}\begin{pmatrix}k^2R^4\sin^2\theta F_1^2+m_sk^2R^4\cos^2 2\theta F_{\mathrm{III}}^2+16x_s^2w^2\sin^6\theta F_1^2\\+16m_sx_s^2w^2\cos^2\theta\sin^4\theta F_{\mathrm{III}}^2+8kx_swR^2\sin 2\theta\sin^3\theta F_1^2\\+8kx_swR^2\cos\theta\cos 2\theta\sin^2\theta F_{\mathrm{III}}^2\end{pmatrix}\alpha\mathrm{d}A^{\mathrm{c}}\bullet\sin^2\gamma
\end{aligned}
\tag{B.2}
$$

$$
\begin{aligned}
g_{33}^{2\sim 1\,\mathrm{c}} &= \frac{\partial u_3^{2\sim 1\,\mathrm{c}}}{\partial P_3^{2\,\mathrm{c}}} \\
&= \frac{2}{E'\pi R^8}\iint_{A^{1\,\mathrm{c}}}(4x_s^2h^2\sin^4\theta F_2^2+4m_sx_s^2h^2\sin^2\theta\cos^2\theta F_{\mathrm{III}}^2+k^2R^4\sin^2\theta F_{\mathrm{II}}^2)\alpha\mathrm{d}A^{\mathrm{c}}\bullet\sin^2\gamma \\
&+ \frac{1}{E'\pi R^8}\iint_{A^{1\,\mathrm{c}}}\begin{pmatrix}4x_skhR^2\sin 2\theta\sin^2\theta F_2^2+4x_sm_skhR^2\sin\theta\cos\theta\cos 2\theta F_{\mathrm{III}}^2\\+16hwx_s^2\sin^5\theta F_1F_2+16m_shwx_s^2\sin^3\theta\cos^2\theta F_{\mathrm{III}}^2\end{pmatrix}\alpha\mathrm{d}A^{\mathrm{c}}\bullet(-\sin\gamma\cos\gamma) \\
&+ \frac{2}{E'\pi R^8}\iint_{A^{1\,\mathrm{c}}}\begin{pmatrix}k^2R^4\sin^2\theta F_1^2+m_sk^2R^4\cos^2 2\theta F_{\mathrm{III}}^2+16x_s^2w^2\sin^6\theta F_1^2\\+16m_sx_s^2w^2\cos^2\theta\sin^4\theta F_{\mathrm{III}}^2+8kx_swR^2\sin 2\theta\sin^3\theta F_1^2\\+8kx_swR^2\cos\theta\cos 2\theta\sin^2\theta F_{\mathrm{III}}^2\end{pmatrix}\alpha\mathrm{d}A^{\mathrm{c}}\bullet\cos^2\gamma
\end{aligned}
\tag{B.3}
$$

$$
\begin{aligned}
g_{44}^{2\sim 1\,\mathrm{c}} &= \frac{\partial u_4^{2\sim 1\,\mathrm{c}}}{\partial P_4^{2\,\mathrm{c}}} \\
&= \frac{2}{E'\pi R^8}\iint_{A^{1\,\mathrm{c}}}(h^2\sin^2 2\theta F_2^2+m_sh^2\cos^2 2\theta F_{\mathrm{III}}^2+4w^2\sin^4\theta F_{\mathrm{II}}^2)\alpha\mathrm{d}A^{\mathrm{c}}
\end{aligned}
\tag{B.4}
$$

$$
\begin{aligned}
g_{55}^{2\sim 1\,\mathrm{c}} &= \frac{\partial u_5^{2\sim 1\,\mathrm{c}}}{\partial P_5^{2\,\mathrm{c}}} \\
&= \frac{2}{E'\pi R^8}\iint_{A^{1\,\mathrm{c}}}(16w^2\sin^6\theta F_1^2+16m_sw^2\cos^2\theta\sin^4\theta F_{\mathrm{III}}^2)\alpha\mathrm{d}A^{\mathrm{c}}\bullet\cos^2\gamma \\
&+ \frac{-1}{E'\pi R^8}\iint_{A^{1\,\mathrm{c}}}(16hw\sin^5\theta F_1F_2+16m_shw\cos^2\theta\sin^3\theta F_{\mathrm{III}}^2)\alpha\mathrm{d}A^{\mathrm{c}}\bullet\sin\gamma\cos\gamma \\
&+ \frac{2}{E'\pi R^8}\iint_{A^{1\,\mathrm{c}}}(4h^2\sin^4\theta F_2^2+4m_sh^2\sin^2\theta\cos^2\theta F_{\mathrm{III}}^2)\alpha\mathrm{d}A^{\mathrm{c}}\bullet\sin^2\gamma
\end{aligned}
\tag{B.5}
$$

$$
\begin{aligned}
g_{66}^{2\sim 1\,\mathrm{c}} &= \frac{\partial u_6^{2\sim 1\,\mathrm{c}}}{\partial P_6^{2\,\mathrm{c}}} \\
&= \frac{2}{E'\pi R^8}\iint_{A^{1\,\mathrm{c}}}(16w^2\sin^6\theta F_1^2 + 16m_s w^2\cos^2\theta\sin^4\theta F_{\mathrm{III}}^2)\alpha\mathrm{d}A^{\mathrm{c}}\bullet\sin^2\gamma \\
&+ \frac{-1}{E'\pi R^8}\iint_{A^{1\,\mathrm{c}}}(16hw\sin^5\theta F_1F_2 + 16m_s hw\cos^2\theta\sin^3\theta F_{\mathrm{III}}^2)\alpha\mathrm{d}A^{\mathrm{c}}\bullet(-\sin\gamma\cos\gamma) \\
&+ \frac{2}{E'\pi R^8}\iint_{A^{1\,\mathrm{c}}}(4h^2\sin^4\theta F_2^2 + 4m_s h^2\sin^2\theta\cos^2\theta F_{\mathrm{III}}^2)\alpha\mathrm{d}A^{\mathrm{c}}\bullet\cos^2\gamma
\end{aligned}
\tag{B.6}
$$

$$
\begin{aligned}
g_{12}^{2\sim 1\,\mathrm{c}} &= \frac{\partial u_1^{2\sim 1\,\mathrm{c}}}{\partial P_2^{2\,\mathrm{c}}} \\
&= \frac{1}{E'\pi R^6}\iint_{A^{1\,\mathrm{c}}}(4x_s h\sin^4\theta F_1F_2 + 4m_s x_s h\sin^2\theta\cos^2\theta F_{\mathrm{III}}^2)\alpha\mathrm{d}A^{\mathrm{c}}\bullet\cos\gamma \\
&+ \frac{1}{E'\pi R^6}\iint_{A^{1\,\mathrm{c}}}\begin{pmatrix}2kR^2\sin 2\theta\sin^2\theta F_1^2 + 2kR^2\sin\theta\cos\theta\cos 2\theta F_{\mathrm{III}}^2 \\ +8x_s w\sin^5\theta F_1^2 + 8x_s m_s w\sin^3\theta\cos^2\theta F_{\mathrm{III}}^2\end{pmatrix}\alpha\mathrm{d}A^{\mathrm{c}}\bullet\sin\gamma
\end{aligned}
\tag{B.7}
$$

$$
\begin{aligned}
g_{13}^{2\sim 1\,\mathrm{c}} &= \frac{\partial u_1^{2\sim 1\,\mathrm{c}}}{\partial P_3^{2\,\mathrm{c}}} \\
&= \frac{1}{E'\pi R^6}\iint_{A^{1\,\mathrm{c}}}(4x_s h\sin^4\theta F_1F_2 + 4m_s x_s h\sin^2\theta\cos^2\theta F_{\mathrm{III}}^2)\alpha\mathrm{d}A^{\mathrm{c}}\bullet(-\sin\gamma) \\
&+ \frac{1}{E'\pi R^6}\iint_{A^{1\,\mathrm{c}}}\begin{pmatrix}2kR^2\sin 2\theta\sin^2\theta F_1^2 + 2kR^2\sin\theta\cos\theta\cos 2\theta F_{\mathrm{III}}^2 \\ +8x_s w\sin^5\theta F_1^2 + 8x_s m_s w\sin^3\theta\cos^2\theta F_{\mathrm{III}}^2\end{pmatrix}\alpha\mathrm{d}A^{\mathrm{c}}\bullet\cos\gamma
\end{aligned}
\tag{B.8}
$$

$$
\begin{aligned}
g_{14}^{2\sim 1\,\mathrm{c}} &= \frac{\partial u_1^{2\sim 1\,\mathrm{c}}}{\partial P_4^{2\,\mathrm{c}}} \\
&= \frac{1}{E'\pi R^6}\iint_{A^{1\,\mathrm{c}}}(2h\sin 2\theta\sin^2\theta F_1F_2 + 2m_s h\sin\theta\cos\theta\cos 2\theta F_{\mathrm{III}}^2)\alpha\mathrm{d}A^{\mathrm{c}}
\end{aligned}
\tag{B.9}
$$

$$
\begin{aligned}
g_{15}^{2\sim 1\,\mathrm{c}} &= \frac{\partial u_1^{2\sim 1\,\mathrm{c}}}{\partial P_5^{2\,\mathrm{c}}} \\
&= \frac{2}{E'\pi R^6}\iint_{A^{1\,\mathrm{c}}}(8w\sin^5\theta F_1^2 + 8m_s w\cos^2\theta\sin^3\theta F_{\mathrm{III}}^2)\alpha\mathrm{d}A^{\mathrm{c}}\bullet\cos\gamma \\
&+ \frac{-1}{E'\pi R^6}\iint_{A^{1\,\mathrm{c}}}(4h\sin^4\theta F_1F_2 + 4m_s h\sin^2\theta\cos^2\theta F_{\mathrm{III}}^2)\alpha\mathrm{d}A^{\mathrm{c}}\bullet\sin\gamma
\end{aligned}
\tag{B.10}
$$

$$g_{16}^{2\sim 1\,\mathrm{c}}=\frac{\partial u_1^{2\sim 1\,\mathrm{c}}}{\partial P_6^{2\,\mathrm{c}}}$$

$$=\frac{2}{E'\pi R^6}\iint_{A^{1\,\mathrm{c}}}(8w\sin^5\theta F_1^2+8m_s w\cos^2\theta\sin^3\theta F_{\mathrm{III}}^2)\alpha\mathrm{d}A^{\mathrm{c}}\bullet(-\sin\gamma)$$

$$+\frac{-1}{E'\pi R^6}\iint_{A^{1\,\mathrm{c}}}(4h\sin^4\theta F_1F_2+4m_s h\sin^2\theta\cos^2\theta F_{\mathrm{III}}^2)\alpha\mathrm{d}A^{\mathrm{c}}\bullet\cos\gamma \tag{B.11}$$

$$g_{23}^{2\sim 1\,\mathrm{c}}=\frac{\partial u_2^{2\sim 1\,\mathrm{c}}}{\partial P_3^{2\,\mathrm{c}}}$$

$$=\frac{2}{E'\pi R^8}\iint_{A^{1\,\mathrm{c}}}(4x_s^2h^2\sin^4\theta F_2^2+4m_s x_s^2h^2\sin^2\theta\cos^2\theta F_{\mathrm{III}}^2+k^2R^4\sin^2\theta F_{\mathrm{II}}^2)\alpha\mathrm{d}A^{\mathrm{c}}\bullet(-\sin\gamma\cos\gamma)$$

$$+\frac{1}{E'\pi R^8}\iint_{A^{1\,\mathrm{c}}}\begin{pmatrix}4x_skhR^2\sin 2\theta\sin^2\theta F_2^2+4x_sm_skhR^2\sin\theta\cos\theta\cos 2\theta F_{\mathrm{III}}^2\\+16hwx_s^2\sin^5\theta F_1F_2+16m_shwx_s^2\sin^3\theta\cos^2\theta F_{\mathrm{III}}^2\end{pmatrix}\alpha\mathrm{d}A^{\mathrm{c}}\bullet\cos^2\gamma$$

$$+\frac{2}{E'\pi R^8}\iint_{A^{1\,\mathrm{c}}}\begin{pmatrix}k^2R^4\sin^2\theta F_1^2+m_sk^2R^4\cos^2 2\theta F_{\mathrm{III}}^2+16x_s^2w^2\sin^6\theta F_1^2\\+16m_sx_s^2w^2\cos^2\theta\sin^4\theta F_{\mathrm{III}}^2+8kx_swR^2\sin 2\theta\sin^3\theta F_1^2\\+8kx_swR^2\cos\theta\cos 2\theta\sin^2\theta F_{\mathrm{III}}^2\end{pmatrix}\alpha\mathrm{d}A^{\mathrm{c}}\bullet\sin\gamma\cos\gamma \tag{B.12}$$

$$g_{24}^{2\sim 1\,\mathrm{c}}=\frac{\partial u_2^{2\sim 1\,\mathrm{c}}}{\partial P_4^{2\,\mathrm{c}}}$$

$$=\frac{1}{E'\pi R^8}\iint_{A^{1\,\mathrm{c}}}\begin{pmatrix}4x_sh^2\sin 2\theta\sin^2\theta F_2^2+4x_sm_sh^2\sin\theta\cos\theta\cos 2\theta F_{\mathrm{III}}^2\\+4kwR^2\sin^3\theta F_{\mathrm{II}}^2\end{pmatrix}\alpha\mathrm{d}A^{\mathrm{c}}\bullet\cos\gamma \tag{B.13}$$

$$+\frac{1}{E'\pi R^8}\iint_{A^{1\,\mathrm{c}}}\begin{pmatrix}8x_shw\sin 2\theta\sin^2\theta F_1F_2+8x_sm_shw\cos\theta\cos 2\theta\sin^2\theta F_{\mathrm{III}}^2\\+2khR^2\sin^2 2\theta F_1F_2+2m_skhR^2\cos^2 2\theta F_{\mathrm{III}}^2\end{pmatrix}\alpha\mathrm{d}A^{\mathrm{c}}\bullet\sin\gamma$$

$$g_{25}^{2\sim 1\,\mathrm{c}}=\frac{\partial u_2^{2\sim 1\,\mathrm{c}}}{\partial P_5^{2\,\mathrm{c}}}$$

$$=\frac{1}{E'\pi R^8}\iint_{A^{1\,\mathrm{c}}}(16x_shw\sin^5\theta F_1F_2+16x_sm_shw\cos^2\theta\sin^3\theta F_{\mathrm{III}}^2)\alpha\mathrm{d}A^{\mathrm{c}}\bullet\cos^2\gamma$$

$$+\frac{-2}{E'\pi R^8}\iint_{A^{1\,\mathrm{c}}}(4x_sh^2\sin^4\theta F_2^2+4x_sm_sh^2\sin^2\theta\cos^2\theta F_{\mathrm{III}}^2)\alpha\mathrm{d}A^{\mathrm{c}}\bullet\sin\gamma\cos\gamma \tag{B.14}$$

$$+\frac{1}{E'\pi R^8}\iint_{A^{1\,\mathrm{c}}}\begin{pmatrix}8kwR^2\sin 2\theta\sin^3\theta F_1^2+8m_skwR^2\cos\theta\cos 2\theta\sin^2\theta F_{\mathrm{III}}^2\\+32x_sw^2\sin^6\theta F_1^2+32x_sm_sw^2\cos^2\theta\sin^4\theta F_{\mathrm{III}}^2\end{pmatrix}\alpha\mathrm{d}A^{\mathrm{c}}\bullet\sin\gamma\cos\gamma$$

$$+\frac{-1}{E'\pi R^8}\iint_{A^{1\,\mathrm{c}}}\begin{pmatrix}4khR^2\sin 2\theta\sin^2\theta F_1F_2+4m_skhR^2\sin\theta\cos\theta\cos 2\theta F_{\mathrm{III}}^2\\+16x_shw\sin^5\theta F_1F_2+16x_sm_shw\sin^3\theta\cos^2\theta F_{\mathrm{III}}^2\end{pmatrix}\alpha\mathrm{d}A^{\mathrm{c}}\bullet\sin^2\gamma$$

$$
\begin{aligned}
g_{26}^{2\sim 1\,\mathrm{c}} &= \frac{\partial u_2^{2\sim 1\,\mathrm{c}}}{\partial P_6^{2\,\mathrm{c}}} \\
&= \frac{1}{E'\pi R^8}\iint_{A^{1\,\mathrm{c}}}(16x_s hw\sin^5\theta F_1F_2 + 16x_s m_s hw\cos^2\theta\sin^3\theta F_{\mathrm{III}}^2)\alpha\mathrm{d}A^{\mathrm{c}}\bullet(-\sin\gamma\cos\gamma) \\
&+ \frac{-2}{E'\pi R^8}\iint_{A^{1\,\mathrm{c}}}(4x_s h^2\sin^4\theta F_2^2 + 4x_s m_s h^2\sin^2\theta\cos^2\theta F_{\mathrm{III}}^2)\alpha\mathrm{d}A^{\mathrm{c}}\bullet\cos^2\gamma \\
&+ \frac{1}{E'\pi R^8}\iint_{A^{1\,\mathrm{c}}}\begin{pmatrix}8kwR^2\sin 2\theta\sin^3\theta F_1^2 + 8m_s kwR^2\cos\theta\cos 2\theta\sin^2\theta F_{\mathrm{III}}^2 \\ +32x_s w^2\sin^6\theta F_1^2 + 32x_s m_s w^2\cos^2\theta\sin^4\theta F_{\mathrm{III}}^2\end{pmatrix}\alpha\mathrm{d}A^{\mathrm{c}}\bullet(-\sin^2\gamma) \\
&+ \frac{-1}{E'\pi R^8}\iint_{A^{1\,\mathrm{c}}}\begin{pmatrix}4khR^2\sin 2\theta\sin^2\theta F_1F_2 + 4m_s khR^2\sin\theta\cos\theta\cos 2\theta F_{\mathrm{III}}^2 \\ +16x_s hw\sin^5\theta F_1F_2 + 16x_s m_s hw\sin^3\theta\cos^2\theta F_{\mathrm{III}}^2\end{pmatrix}\alpha\mathrm{d}A^{\mathrm{c}}\bullet\sin\gamma\cos\gamma
\end{aligned}
$$

$$
\begin{aligned}
g_{34}^{2\sim 1\,\mathrm{c}} &= \frac{\partial u_3^{2\sim 1\,\mathrm{c}}}{\partial P_4^{2\,\mathrm{c}}} \\
&= \frac{1}{E'\pi R^8}\iint_{A^{1\,\mathrm{c}}}\begin{pmatrix}4x_s h^2\sin 2\theta\sin^2\theta F_2^2 + 4x_s m_s h^2\sin\theta\cos\theta\cos 2\theta F_{\mathrm{III}}^2 \\ +4kwR^2\sin^3\theta F_{\mathrm{II}}^2\end{pmatrix}\alpha\mathrm{d}A^{\mathrm{c}}\bullet(-\sin\gamma) \\
&+ \frac{1}{E'\pi R^8}\iint_{A^{1\,\mathrm{c}}}\begin{pmatrix}8x_s hw\sin 2\theta\sin^2\theta F_1F_2 + 8x_s m_s hw\cos\theta\cos 2\theta\sin^2\theta F_{\mathrm{III}}^2 \\ +2khR^2\sin^2 2\theta F_1F_2 + 2m_s khR^2\cos^2 2\theta F_{\mathrm{III}}^2\end{pmatrix}\alpha\mathrm{d}A^{\mathrm{c}}\bullet\cos\gamma
\end{aligned}
$$

$$
\begin{aligned}
g_{35}^{2\sim 1\,\mathrm{c}} &= \frac{\partial u_3^{2\sim 1\,\mathrm{c}}}{\partial P_5^{2\,\mathrm{c}}} \\
&= \frac{1}{E'\pi R^8}\iint_{A^{1\,\mathrm{c}}}(16x_s hw\sin^5\theta F_1F_2 + 16x_s m_s hw\cos^2\theta\sin^3\theta F_{\mathrm{III}}^2)\alpha\mathrm{d}A^{\mathrm{c}}\bullet(-\sin\gamma\cos\gamma) \\
&+ \frac{-2}{E'\pi R^8}\iint_{A^{1\,\mathrm{c}}}(4x_s h^2\sin^4\theta F_2^2 + 4x_s m_s h^2\sin^2\theta\cos^2\theta F_{\mathrm{III}}^2)\alpha\mathrm{d}A^{\mathrm{c}}\bullet(-\sin^2\gamma) \\
&+ \frac{1}{E'\pi R^8}\iint_{A^{1\,\mathrm{c}}}\begin{pmatrix}8kwR^2\sin 2\theta\sin^3\theta F_1^2 + 8m_s kwR^2\cos\theta\cos 2\theta\sin^2\theta F_{\mathrm{III}}^2 \\ +32x_s w^2\sin^6\theta F_1^2 + 32x_s m_s w^2\cos^2\theta\sin^4\theta F_{\mathrm{III}}^2\end{pmatrix}\alpha\mathrm{d}A^{\mathrm{c}}\bullet\cos^2\gamma \\
&+ \frac{-1}{E'\pi R^8}\iint_{A^{1\,\mathrm{c}}}\begin{pmatrix}4khR^2\sin 2\theta\sin^2\theta F_1F_2 + 4m_s khR^2\sin\theta\cos\theta\cos 2\theta F_{\mathrm{III}}^2 \\ +16x_s hw\sin^5\theta F_1F_2 + 16x_s m_s hw\sin^3\theta\cos^2\theta F_{\mathrm{III}}^2\end{pmatrix}\alpha\mathrm{d}A^{\mathrm{c}}\bullet\sin\gamma\cos\gamma
\end{aligned}
$$

(B.15)

(B.16)

(B.17)

$$
\begin{aligned}
g_{36}^{2\sim 1\,\mathrm{c}} &= \frac{\partial u_3^{2\sim 1\,\mathrm{c}}}{\partial P_6^{2\,\mathrm{c}}} \\
&= \frac{1}{E'\pi R^8}\iint_{A^{1\,\mathrm{c}}}(16x_s hw\sin^5\theta F_1F_2 + 16x_s m_s hw\cos^2\theta\sin^3\theta F_{\mathrm{III}}^2)\alpha \mathrm{d}A^{\mathrm{c}}\bullet\sin^2\gamma \\
&+ \frac{-2}{E'\pi R^8}\iint_{A^{1\,\mathrm{c}}}(4x_s h^2\sin^4\theta F_2^2 + 4x_s m_s h^2\sin^2\theta\cos^2\theta F_{\mathrm{III}}^2)\alpha \mathrm{d}A^{\mathrm{c}}\bullet(-\sin\gamma\cos\gamma) \\
&+ \frac{1}{E'\pi R^8}\iint_{A^{1\,\mathrm{c}}}\begin{pmatrix}8kwR^2\sin 2\theta\sin^3\theta F_1^2 + 8m_s kwR^2\cos\theta\cos 2\theta\sin^2\theta F_{\mathrm{III}}^2 \\ +32x_s w^2\sin^6\theta F_1^2 + 32x_s m_s w^2\cos^2\theta\sin^4\theta F_{\mathrm{III}}^2\end{pmatrix}\alpha \mathrm{d}A^{\mathrm{c}}\bullet(-\sin\gamma\cos\gamma) \\
&+ \frac{-1}{E'\pi R^8}\iint_{A^{1\,\mathrm{c}}}\begin{pmatrix}4khR^2\sin 2\theta\sin^2\theta F_1F_2 + 4m_s khR^2\sin\theta\cos\theta\cos 2\theta F_{\mathrm{III}}^2 \\ +16x_s hw\sin^5\theta F_1F_2 + 16x_s m_s hw\sin^3\theta\cos^2\theta F_{\mathrm{III}}^2\end{pmatrix}\alpha \mathrm{d}A^{\mathrm{c}}\bullet\cos^2\gamma
\end{aligned}
\tag{B.18}
$$

$$
\begin{aligned}
g_{45}^{2\sim 1\,\mathrm{c}} &= \frac{\partial u_4^{2\sim 1\,\mathrm{c}}}{\partial P_5^{2\,\mathrm{c}}} \\
&= \frac{1}{E'\pi R^8}\iint_{A^{1\,\mathrm{c}}}(8hw\sin 2\theta\sin^3\theta F_1F_2 + 8m_s hw\cos\theta\cos 2\theta\sin^2\theta F_{\mathrm{III}}^2)\alpha \mathrm{d}A^{\mathrm{c}}\bullet\cos\gamma \\
&+ \frac{-1}{E'\pi R^8}\iint_{A^{1\,\mathrm{c}}}(4h^2\sin 2\theta\sin^2\theta F_2^2 + 4m_s h^2\sin\theta\cos\theta\cos 2\theta F_{\mathrm{III}}^2)\alpha \mathrm{d}A^{\mathrm{c}}\bullet\sin\gamma
\end{aligned}
\tag{B.19}
$$

$$
\begin{aligned}
g_{46}^{2\sim 1\,\mathrm{c}} &= \frac{\partial u_4^{2\sim 1\,\mathrm{c}}}{\partial P_6^{2\,\mathrm{c}}} \\
&= \frac{1}{E'\pi R^8}\iint_{A^{1\,\mathrm{c}}}(8hw\sin 2\theta\sin^3\theta F_1F_2 + 8m_s hw\cos\theta\cos 2\theta\sin^2\theta F_{\mathrm{III}}^2)\alpha \mathrm{d}A^{\mathrm{c}}\bullet(-\sin\gamma) \\
&+ \frac{-1}{E'\pi R^8}\iint_{A^{1\,\mathrm{c}}}(4h^2\sin 2\theta\sin^2\theta F_2^2 + 4m_s h^2\sin\theta\cos\theta\cos 2\theta F_{\mathrm{III}}^2)\alpha \mathrm{d}A^{\mathrm{c}}\bullet\cos\gamma
\end{aligned}
\tag{B.20}
$$

$$
\begin{aligned}
g_{56}^{2\sim 1\,\mathrm{c}} &= \frac{\partial u_5^{2\sim 1\,\mathrm{c}}}{\partial P_6^{2\,\mathrm{c}}} \\
&= \frac{2}{E'\pi R^8}\iint_{A^{1\,\mathrm{c}}}(16w^2\sin^6\theta F_1^2 + 16m_s w^2\cos^2\theta\sin^4\theta F_{\mathrm{III}}^2)\alpha \mathrm{d}A^{\mathrm{c}}\bullet(-\sin\gamma\cos\gamma) \\
&+ \frac{-1}{E'\pi R^8}\iint_{A^{1\,\mathrm{c}}}(16hw\sin^5\theta F_1F_2 + 16m_s hw\cos^2\theta\sin^3\theta F_{\mathrm{III}}^2)\alpha \mathrm{d}A^{\mathrm{c}}\bullet\cos^2\gamma \\
&+ \frac{2}{E'\pi R^8}\iint_{A^{1\,\mathrm{c}}}(4h^2\sin^4\theta F_2^2 + 4m_s h^2\sin^2\theta\cos^2\theta F_{\mathrm{III}}^2)\alpha \mathrm{d}A^{\mathrm{c}}\bullet\sin\gamma\cos\gamma
\end{aligned}
\tag{B.21}
$$

And it can be obtained that

$$
g_{ij}^{2\sim 1\,\mathrm{c}} = g_{ji}^{2\sim 1\,\mathrm{c}} \tag{B.22}
$$

References

1. A.W. Lees, J.K. Sinha, M.I. Friswell, Model-based identification of rotating machines, Mech Syst Signal Pr, 23 (6) (2009) 1884-1893.
2. D. Goyal, B.S. Pabla, The Vibration Monitoring Methods and Signal Processing Techniques for

Structural Health Monitoring: A Review, Arch Comput Method E, 23 (4) (2016) 585-594.

3. R. Liu, B. Yang, E. Zio, X. Chen, Artificial intelligence for fault diagnosis of rotating machinery: A review, Mech Syst Signal Pr, 108 (2018) 33-47.
4. N. Kushwaha, V.N. Patel, Modelling and analysis of a cracked rotor: a review of the literature and its implications, Arch Appl Mech, 90 (6) (2020) 1215-1245.
5. A.S. Sekhar, Crack identification in a rotor system: A model-based approach, J Sound Vib, 270 (2004) 887-902.
6. P. Pennacchi, N. Bachschmid, A. Vania, A model-based identification method of transverse cracks in rotating shafts suitable for industrial machines, Mech Syst Signal Pr, 20 (2006) 2112-2147.
7. S. Singh, R. Tiwari, Model based identification of crack and bearing dynamic parameters in flexible rotor systems supported with an auxiliary active magnetic bearing, Mech Mach Theory, 122 (2018) 292-307.
8. N.T. Khiem, T.V. Lien, A simplified method for natural frequency analysis of a multiple cracked beam, J Sound Vib, 245 (4) (2001) 737-751.
9. S. El Arem, Nonlinear analysis, instability and routes to chaos of a cracked rotating shaft, Nonlinear Dynam, (2019).
10. H.B. Dong, X.F. Chen, B. Li, K.Y. Qi, Z.J. He, Rotor crack detection based on high-precision modal parameter identification method and wavelet finite element model, Mech Syst Signal Pr, 23 (2009) 869-883.
11. A. Morassi, M. Rollo, Identification of two cracks in a simply supported beam from minimal frequency measurements, J Vib Control, 7 (5) (2001) 729-739.
12. D.P. Patil, S.K. Maiti, Detection of multiple cracks using frequency measurements, Eng Fract Mech, 70 (12) (2003) 1553-1572.
13. J. Lee, Identification of multiple cracks in a beam using vibration amplitudes, J Sound Vib, 326 (1) (2009) 205-212.
14. M.A. AL-Shudeifat, Stability analysis and backward whirl investigation of cracked rotors with time-varying stiffness, J Sound Vib, 348 (2015) 365-380.
15. H. Khorrami, S. Rakheja, R. Sedaghati, Vibration behavior of a two-crack shaft in a rotor disc-bearing system, Mech Mach Theory, 113 (2017) 67-84.
16. B. Zhang, Y. Li, Six degrees of freedom coupled dynamic response of rotor with a transverse breathing crack, Nonlinear Dynam, 78 (3) (2014) 1843-1861.
17. C. Fu, X. Ren, Y. Yang, K. Lu, Y. Wang, Nonlinear response analysis of a rotor system with a transverse breathing crack under interval uncertainties, Int J Nonlin Mech, 105 (2018) 77-87.
18. A.K. Darpe, K. Gupta, A. Chawla, Dynamics of a two-crack rotor, J Sound Vib, 259 (3) (2003) 649-675.
19. L. Xiang, Y. Zhang, A. Hu, Crack characteristic analysis of multi-fault rotor system based on whirl orbits, Nonlinear Dynam, 95 (4) (2019) 2675-2690.
20. R. Gradzki, Z. Kulesza, B. Bartoszewicz, Method of shaft crack detection based on squared gain of vibration amplitude, Nonlinear Dynam, 98 (1) (2019) 671-690.
21. Z.N. Haji, S. Olutunde Oyadiji, The use of roving discs and orthogonal natural frequencies for crack identification and location in rotors, J Sound Vib, 333 (23) (2014) 6237-6257.
22. A.S. Sekhar, Model-based identification of two cracks in a rotor system, Mech Syst Signal Pr, 18 (4) (2004) 977-983.
23. S. El Arem, On the mechanics of beams and shafts with cracks: A standard and generic approach, European Journal of Mechanics - A/Solids, 85 (2021) 104088.

24. D. Li, Z. Xu, W. Ostachowicz, M. Cao, J. Liu, Identification of multiple cracks in noisy conditions using scale-correlation-based multiscale product of SWPT with laser vibration measurement, Mech Syst Signal Pr, 145 (2020) 106889.
25. X. Zhao, Y.R. Zhao, X.Z. Gao, X.Y. Li, Y.H. Li, Green′s functions for the forced vibrations of cracked Euler–Bernoulli beams, Mech Syst Signal Pr, 68-69 (2016) 155-175.
26. B. Chen, X. Zhao, Y.H. Li, Y. Guo, Forced vibration analysis of multi-cracked Timoshenko beam with the inclusion of damping by virtue of Green's functions, Appl Acoust, 155 (2019) 477-491.
27. Z. Lu, D. Dong, H. Ouyang, S. Cao, C. Hua, Localization of breathing cracks in stepped rotors using super-harmonic characteristic deflection shapes based on singular value decomposition in frequency domain, Fatigue Fract Eng M, 40 (11) (2017) 1825-1837.
28. A.K. Darpe, Coupled vibrations of a rotor with slant crack, J Sound Vib, 305 (1) (2007) 172-193.
29. N.M. Newmark, A method of computation for structural dynamics, Journal of the Engineering Mechanics Division, 85 (3) (1959) 67-94.
30. A.S. Sekhar, Multiple cracks effects and identification, Mech Syst Signal Pr, 22 (4) (2008) 845-878.
31. C.M. Stoisser, S. Audebert, A comprehensive theoretical, numerical and experimental approach for crack detection in power plant rotating machinery, Mech Syst Signal Pr, 22 (4) (2008) 818-844.
32. L. Hou, Y. Chen, Q. Cao, Z. Lu, Nonlinear vibration analysis of a cracked rotor-ball bearing system during flight maneuvers, Mech Mach Theory, 105 (2016) 515-528.
33. V. Gupta, M. Mittal, A novel method of cardiac arrhythmia detection in electrocardiogram signal, International Journal of Medical Engineering and Informatics, 12 (2020) 489.
34. V. Gupta, M. Mittal, V. Mittal, N.K. Saxena, BP Signal Analysis Using Emerging Techniques and its Validation Using ECG Signal, Sensing and Imaging, 22 (1) (2021) 25.
35. V. Gupta, M. Mittal, V. Mittal, Chaos Theory and ARTFA: Emerging Tools for Interpreting ECG Signals to Diagnose Cardiac Arrhythmias, Wireless Pers Commun, 118 (4) (2021) 3615-3646.
36. V. Gupta, M. Mittal, QRS Complex Detection Using STFT, Chaos Analysis, and PCA in Standard and Real-Time ECG Databases, Journal of The Institution of Engineers (India): Series B, 100 (5) (2019) 489-497.
37. V. Gupta, M. Mittal, V. Mittal, R-peak detection based chaos analysis of ECG signal, Analog Integr Circ S, 102 (3) (2020) 479-490.
38. V. Gupta, M. Mittal, V. Mittal, R-Peak Detection Using Chaos Analysis in Standard and Real Time ECG Databases, Irbm, 40 (6) (2019) 341-354.
39. C. Guo, M.A. Al-Shudeifat, J. Yan, L.A. Bergman, D.M. Mcfarland, E.A. Butcher, C. Guo, Application of empirical mode decomposition to a Jeffcott rotor with a breathing crack, J Sound Vib, 332 (16) (2013) 3881-3892.
40. R. Gasch, Dynamic behaviour of the Laval rotor with a transverse crack, Mech Syst Signal Pr, 22 (4) (2008) 790-804.
41. C. Guo, J. Yan, W. Yang, Crack detection for a Jeffcott rotor with a transverse crack: An experimental investigation, Mech Syst Signal Pr, 83 (2017) 260-271.
42. X. Chen, J. Han, On rotation phase of a rotating machinery by full vector spectrum and its applications, Mechanical Science and Technology, 27 (4) (2008) 515-519.